[Review] The Rise of HgTe Colloidal Quantum Dots for Infrared Optoelectronics

Kseniia Sergeeva, Huichen Zhang, Arsenii Portniagin, Erwan Bossavit, Ge Mu, Stephen Kershaw, Sandrine Ithurria, Philippe Guyot-Sionnest, Sean Keuleyan, Christophe Delerue, et al.

ADVANCED FUNCTIONAL MATERIALS
www.afm-journal.de

The Rise of HgTe Colloidal Quantum Dots for Infrared Optoelectronics

Kseniia A. Sergeeva, Huichen Zhang, Arsenii S. Portniagin, Erwan Bossavit, Ge Mu, Stephen V. Kershaw, Sandrine Ithurria, Philippe Guyot-Sionnest, Sean Keuleyan, Christophe Delerue, Xin Tang, Andrey L. Rogach, and Emmanuel Lhuillier**

Among materials produced as colloidal quantum dots (CQDs), HgTe has a special status being the only material covering the whole infrared range from the visible to the THz (0.7–100 µm). This unique property resulting from its electronic structure, combined with an air stability and a capacity for charge conduction has generated consistent and massive efforts to produce and improve HgTe CQDs over the past two decades. Meanwhile, HgTe CQDs offer an infrared platform more advanced than any other colloidal alternatives in the mid-wave infrared regarding their integration into advanced photonic and optoelectronic applications. Here, the latest developments of HgTe CQDs relative to the material's growth, electron structure modelling, its integration into photonic structures and its transfer as the active material from single element devices toward complex sensors and infrared imagers are reviewed. Finally, a discussion about the potential of this material for industry, rising new challenges beyond economical and production considerations at low technological readiness level, relative to the material and device design, is also included.

1. Introduction

Visible light emitting colloidal quantum dots (CQDs) have made substantial strides over the last three decades, earning great recognition such as the award of the 2023 Chemistry Nobel Prize. However, their wide band gaps challenge their utilization in infrared (IR) photonic and optoelectronic applications. To cater for longer wavelengths, one crucial demand is the presence of narrow energy transitions (whether interband or intraband) that can be readily tuned across a wide range, covering the energy spectrum associated with IR wavelengths.

Mercury telluride (HgTe) CQDs have emerged[1–3] as a special candidate among the potential materials, showcasing their unique advantages and positioning them as a standout IR platform. The characteristics of HgTe make this material a compelling

K. A. Sergeeva, A. S. Portniagin, S. V. Kershaw, A. L. Rogach
Department of Materials Science and Engineering
City University of Hong Kong
83 Tat Chee Avenue, Kowloon, Hong Kong SAR 999077, China
E-mail: andrey.rogach@cityu.edu.hk

H. Zhang, E. Bossavit, E. Lhuillier
CNRS
Institut des NanoSciences de Paris
Sorbonne Université
4 place jussieu, Paris 75005, France
E-mail: el@insp.upmc.fr

G. Mu, X. Tang
School of Optics and Photonics
Beijing Institute of Technology
Beijing 100081, China

G. Mu, X. Tang
Beijing Key Laboratory for Precision Optoelectronic Measurement Instrument and Technology
Beijing 100081, China

G. Mu, X. Tang
Yangtze Delta Region Academy of Beijing Institute of Technology
Jiaxing 314019, China

S. Ithurria
CNRS UMR 8213
Laboratoire de Physique et d'Etude des Matériaux ESPCI
PSL Research University
Sorbonne Université
10 rue Vauquelin, Paris 75005, France

P. Guyot-Sionnest
Department of Chemistry and the James Franck Institute
The University of Chicago
929 East 57th Street, Chicago, Illinois 60637, USA

S. Keuleyan
Keuleyanscientific
Eugene, Oregon 97403, USA

C. Delerue
UMR 8520 – IEMN
CNRS
Polytechnique Hauts-de-France
Université Lille
Université Junia
F-59000, Lille 59160, France

The ORCID identification number(s) for the author(s) of this article can be found under https://doi.org/10.1002/adfm.202405307

DOI: 10.1002/adfm.202405307

choice for IR applications due to its narrow energy transition capabilities and versatile tunability across the whole IR energy spectrum. In particular, several distinctive properties of HgTe make it an excellent ma for fulfilling the requirements necessary for effective utilization in IR photonic and optoelectronic applications:

1) **Bulk electronic structure**: Bulk crystalline HgTe boasts a well-investigated electronic nature. Its utilization in applied sciences, especially within HgCdTe alloys for IR sensing,[4] has made it one of the most studied materials. Moreover, its semimetal nature, limited to only a handful of other materials, is characterized by an inverted band ordering at the critical point in the Brillouin zone, which also contributed to its initial investigation as a topological insulator.[5–7] Additionally, being a II-VI semiconductor, it has benefited from advancements in synthetic methodologies achieved with cadmium chalcogenide CQDs.
2) **Spectral tunability**: HgTe is unparalleled among any other semiconductor CQDs in terms of spectral tunability. Its first (band edge) optical feature can span an incredibly wide range, all the way from the visible[8] to the THz range.[9–11] This remarkable property stems directly from its semimetallic bulk nature, allowing for vanishingly small band gaps and much reduced electron and hole effective masses.
3) **Air stability**: HgTe CQDs offer a reasonable air stability, enabling processing of this material in open air while retaining its photoconductive properties. Although limited by ligand oxidation and their subsequent degradation,[12] this advantage is particularly significant compared to lead chalcogenides and narrow band gap III-V materials that require meticulous air-free handling throughout synthesis, purification and device fabrication steps.
4) **Mature surface chemistry**: Surface chemistry modification for HgTe CQDs has been well-developed, allowing solutions of HgTe nanocrystals to be processed akin to infrared photoconductive resists.[13,14] This control facilitates interparticle coupling,[13] doping,[15] and the production of mirror-like quality films with adjustable thicknesses.[14] This maturity in surface chemistry enables precise control and manipulation of the material's properties, opening avenues for tailored applications.

The comprehensive advantages offered by HgTe CQDs have propelled current developments beyond material-centric topics. They now encompass advanced device developments for light emission and absorption, which we will consider in this review.

There has been a substantial number of publications on mercury chalcogenide (HgX, where X is S, Se, Te) nanocrystals to date (**Figure 1**). The journey began in 1993 with the work of M. Müllenborn et al.[16] which successfully obtained colloidal HgTe CQDs, albeit not stable in the long-term and without reporting their IR emission properties. It wasn't until 1999 when A. Rogach et al.[17] demonstrated the first IR-emitting stable material produced by aqueous synthesis that researchers began to take interest in HgTe CQDs. This breakthrough sparked investigations into the electrical transport properties[18] and electroluminescence[19,20] of HgTe CQDs in 2003 and 2005, respectively. Later on, H. Kim et al.[21] reported the first IR photodetector with a response up to 1.6 µm, and for a considerable period, this group continued to contribute significantly to device-related fields.[22–24] Another advancement occurred in 2006 when M. Kovalenko et al.[25] extended the synthesis of HgTe CQDs from aqueous media to organic solvents, along with a narrow size distribution and, therefore, a narrow band gap energy distribution. The IR photoluminescence (PL) spectral range was expanded to 4 µm, optical spectroscopy being the prevalent characterization technique for assessing the quality of the HgTe CQDs.

The field experienced a notable expansion in 2011 with the extension of the spectral range to the mid-infrared region.[26] This breakthrough led to a rapid surge in publications focused on photodetectors tailored for the short-wavelength IR (SWIR) and mid-wavelength IR (MWIR) spectral ranges.[33–39] During that time, the photocurrent response up to 12 µm was reported,[27] as well as the integration of plasmonic structures into photodiode designs to enhance their figures-of-merit.[28] However, the field encountered a temporary regress around 2015, witnessing a 50% decrease in publications, likely due to the diverted attention toward perovskite nanocrystals following the seminal paper of L. Protesescu et al.[40] In 2016, interest in the field revived with the successful derivation of HgTe nanoplatelets (NPLs) using the cation exchange method by the group of S. Ithurria.[8] This breakthrough opened up new avenues for obtaining bright IR emitters within the mercury chalcogenide family. Since then, there has been an exponential rise in publications related to HgTe CQD-based devices. In 2016, thermal imaging applications[32] were reported for the first time, and since then the focus has gradually shifted to light-emitting devices (LEDs; expanding the emission range to 2 µm)[41] and imaging setups[42–46] based on HgTe CQDs, which take up to 20% of all published reports. Simultaneously, researchers explored strategies to enhance the IR PL of HgTe CQDs through their coupling to bound-states-in-continuum supporting plasmonic structures[47,48] or through the formation of 2D/3D heterostructures.[49]

Overall, the field of HgTe CQDs has experienced significant growth. In 2023 alone, over 30 papers were published, covering various aspects such as material synthesis (e.g., the first wurtzite structured HgTe nanorods: NRs),[31] advanced engineering of photodetector structures (e.g., use of multi-resonant gratings as both an electrode and plasmonic structure),[50] improvement of focal plane array-based imaging systems,[46] deeper theoretical investigations predicting the optical properties in thick nanoplatelets,[7] quantum cascade LEDs based on HgSe/CdSe core-shell CQDs,[51] and more. Although several reviews[1,2] on mercury chalcogenide CQDs have been published, most of them tend to focus on specific aspects, such as synthesis,[52] PL, and mostly photodetector performances.[3,53–55] In this review, our objective is to consolidate the latest achievements in HgTe CQD-based devices, provide a comprehensive theoretical perspective, and address material- and structure-related challenges. The detection part is chosen to be complementary to previous reviews showing the latest development related to the coupling of the material to photonic structures and the transition from single pixel devices to imagers. In addition, an emphasis is placed on the exploration and integration of HgTe CQDs into the optoelectronics industry.

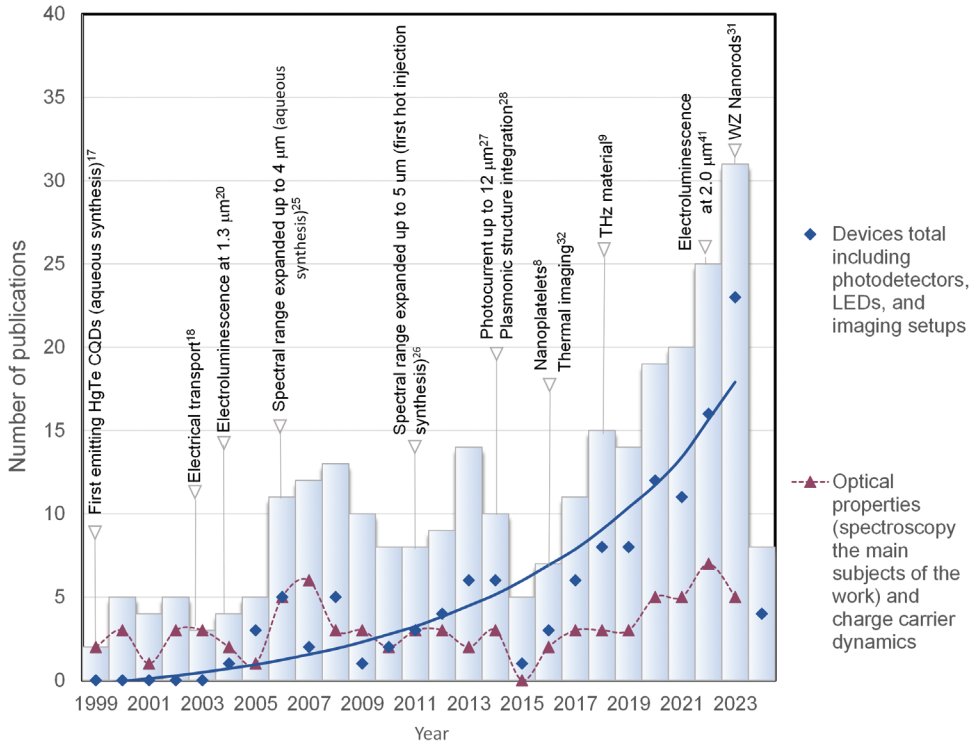

Figure 1. Number of publications on HgTe CQDs through the years according to the Web of Science database. The results were filtered using the following keywords: "HgTe", "mercury chalcogenide", "colloidal quantum dots (nanoplatelets/ nanorods/ nanowires)"; although we appreciate the science made on "quantum wells" or "epitaxial grown HgTe", these keywords were not included. The relevant publications were sorted to the following categories: i) optical properties and charge carrier dynamics (shown with dark pink symbols and a dashed line to guide the eye); ii) devices (shown with dark blue symbols and fitted with a single exponential function); and iii) total number of papers per year across categories i) and ii) (shown with grey bars). Significant milestones in the development of HgTe CQD synthetic procedures, achievements in enhancing of optical properties, and characterization of respective devices, are represented according to references.[8,9,17,18,20,25–28,31,32,41]

2. Material Past and Perspective

The interest in HgTe is certainly driven by the ability of this material to achieve narrow energy transitions suitable for IR wavelengths. The field strongly benefited from a long history of developments relative to the HgCdTe alloy,[4] where the Cd content drives the band gap energy. As this alloy is replaced by quantum-confined forms of HgTe, a similar spectral tunability can be obtained.[56] Though concepts relative to the electronic structure are well established, the transition toward colloidal materials brings new challenges since material parameters are less documented than for their thin film form counterparts. Furthermore, mercury (because of toxicity) and tellurium (because of limited library of precursors) contents have slowed down the exploration for various growth conditions and as a result, the HgTe CQD synthesis remains driven by only a few chemical paths. The growth of Te based nanocrystals is dominated by Te complexed with phosphine (trioctylphosphine telluride being the most used one), a situation that contrasts with S[57] and Se[58] based CQDs growth where a broadening of the precursor library enables a fine tuning of their reactivity. In the case of HgTe, beyond TOPTe, the historical precursor has been H_2Te, whose gaseous character required additional care. This explains why recently the trend has been toward in situ generation of the Te^{2-} ions using precursors such as TMS_2Te (bis(trismethylsilyl)telluride).[59] Regarding mercury precursors, organometallic ones[60] have been banned by all groups due to extreme lethality and liquid mercury[61] tends to be avoided to prevent vapor exposure, thus most efforts are focused on mercury salts.

As the research community has expanded over the recent years, new synthetic procedures[8,61,62] have been proposed enabling concomitant device development. Before going into progress relative to material growth, the obvious toxicity and scarcity of the HgTe compound must be addressed. Mercury is toxic whereas tellurium suffers from limited availability. HgTe for photodetection has currently no alternative among colloidal materials for the MWIR, while it competes with lead-based and III-V semiconductors (InAs and InSb) in the SWIR. The presence of heavy metal is justified in the absence of a safer alternative, and colloidal HgTe comes as replacement of existing toxic bulk semiconductor materials (based on Hg, Cd, As, or Sb). However, the colloidal approach drastically reduces the energy cost related to the growth (no high vacuum, no high temperature) and removes the epitaxial constraint. Regarding the latter point, the use of a toxic lattice matched substrate such as CdZnTe for HgCdTe was the main source of harmful compounds, and this can now be replaced by a silicon CMOS substrate. Certainly, the situation remains non-perfect, but the HgTe CQDs are now mature enough to be applied as spin-coatable inks readily available for advanced devices, so that the focus can be shifted on the optics and device

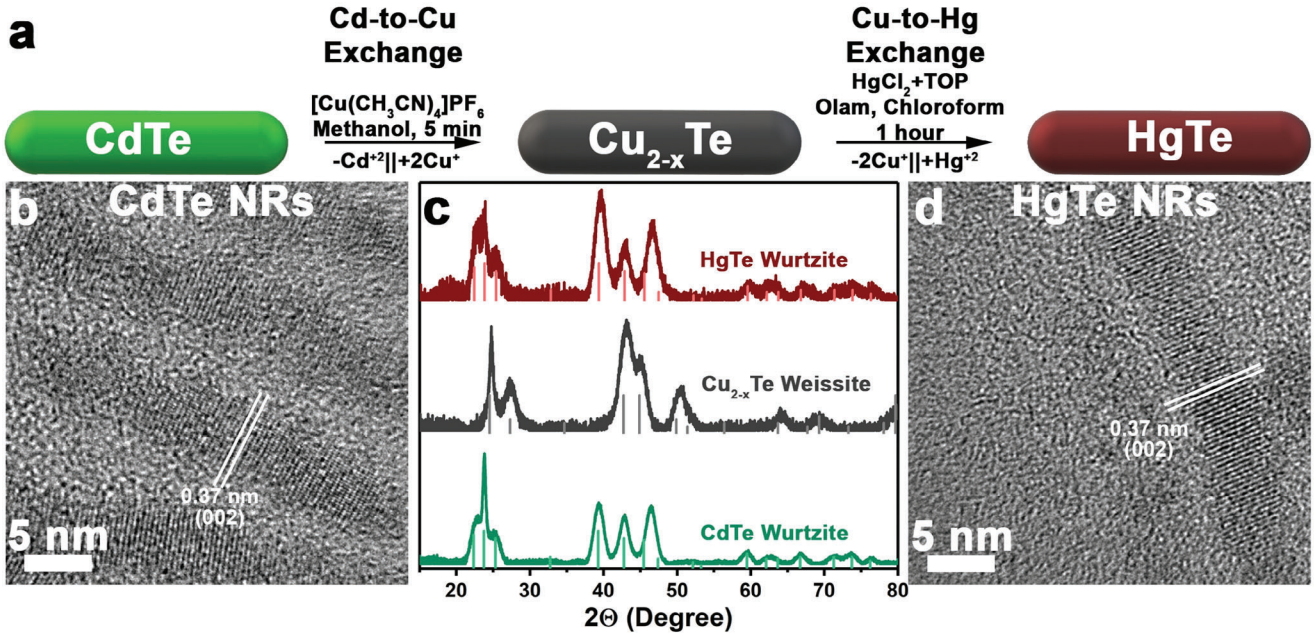

Figure 2. Fabrication of HgTe WZ NRs. a) Two-step cation exchange scheme employed. TOP stands for trioctylphosphine, and Olam for oleylamine; b) High-resolution TEM image of starting CdTe NRs; c) XRD patterns of starting CdTe NRs, intermediate Cu_2Te NRs, and resulting HgTe NRs showing that the initial hexagonal structure was preserved in the latter; d) High-resolution TEM of the obtained WZ HgTe NRs. Adapted with permission from,[31] copyright 2023.

aspects rather than the material issue as it is still the case for III-V alternatives, for example.

2.1. Tuning Electronic Structure Through Shape, Dimensionality and Doping Control

The thermodynamically stable phase of HgTe at low zero pressure is the zinc blende (ZB) phase, and plenty of syntheses of HgTe nanoparticles led to branched morphology,[63,64] raising questions relative to film packing density and its associated impact on carrier mobility. Over the past few years, significant efforts were focused on HgTe particle shape control to obtain spherical one, and to study how the shape impacts their optical and electronic properties, as well as to control dimensionality such as making 2D nanoplatelets[8] and 1D nanorods[31] using a cation exchange procedure.[65,66]

It appears from transmission electron microscopy that the synthetic method of HgTe CQDs conducted in organic solvents lead to non-spherical particle shapes,[59,63,67] with the smallest being branched,[68] and the largest appearing clearly faceted.[26,69] Since the shape was not preventing the emergence of photoluminescence and photoconductive properties, the ma has been left on the side for a while, leaving unaddressed some central questions such as the actual involved facets. This probably has prevented advanced modelling of the electronic structure through density functional theory and the development of more strategies for ligand exchange by design. On a macroscopic level, the non-spherical shape appears unfavorable to achieve films with high volume fractions. S.S. Chee et al. discussed how shape impacts the photoconductive properties of the films.[63] It appears that the CQD shape has a limiting impact on the electron-hole wavefunction overlap and thus on the exciton binding energy, due to the large effective mass of the hole that barely probes the CQD surface. However, it has been pointed out that the low volume fraction is associated with a reduced mobility,[70] as a macroscopic signature of the longer interparticle distance and that the refractive index[6] is reduced due to the presence of voids. To address this problem, new synthetic paths have been proposed. An initial idea has been based on the replacement of TOPTe as the Te precursor for TMS_2Te (bis(trismethylsilyl)telluride), later completed by strategies still based on TOPTe while involving a seed formation step.[62,67,71]

Apart from shape tuning, investigating nanocrystal dimensionality is another leverage for band-structure engineering.[72–75] To overcome the issue with ZB-WZ lattice accommodation raised at the early direct Cd-to-Hg exchange approaches,[8,76–78] an intermediate Cd-to-Cu step was introduced, which allows for the crystal structure, shape and dimensions being preserved (**Figure 2**).[31] This led to the first report of WZ HgTe NRs, offering a new degree of freedom for the design of IR optical features, but also raising a need for theoretical modelling. The final HgTe NRs with aspect ratio (length to diameter) of 10 showed absorption and emission in extended SWIR range, the optical properties being dependent on the residual copper content. Still, two-step cation exchange results in high defect concentration, requiring further synthetic optimization to improve the quality of anisotropic HgTe and devices based on them.

2D-shaped HgTe CQDs, also called NPLs have also been explored.[8,49,77,79] Similar to the NRs, there is still no direct synthesis for their growth and the method also relies on cation exchange, starting this time from CdTe NPLs. The procedure

implies the exposure of the latter to a mercury salt dissolved in oleylamine. It benefits from being conducted slowly (i.e., at low temperature with an excess of ligands) to avoid shape reconstruction as the Cd cations are removed.[77] To date, integration of HgTe NPLs into devices (phototransistors[80] or LEDs)[81] certainly lags behind the 0D counterpart due to the difficultly to obtain high quality films resulting from the reduced colloidal stability of the material. Another limitation is that the two-step growth tends to reduce the amount of materials produced per batch, making the device integration more complicated.

Beyond the shape and dimensionality, doping also dramatically impacts the basic material properties such as carrier dynamics[36] or the spectrum through the emergence of intraband transitions.[59] Various strategies have been explored. A possible active method relies on the use of gates, which can be obtained from dielectric,[13,39,63,82] electrolyte[36,80] or other high capacitance solids.[83,84] A possible derivative of this method is remotely induced doping where the substrate is impacting the actual nature of the majority carrier. In the case of HgTe CQDs, this has been achieved by coupling them to ferroelectric materials,[85,86] or through functionalization of wafers by charge selective transport layers[87] (SnO_2 and Ag_2Te). Compared to gates, the passive method has the advantage of not introducing any additional electrodes, which may behave as a possible non-intrinsic noise source. Complementarily, the doping can also be achieved directly at the nanocrystal level. CQD size drives the nature of the majority carrier with a transition from p-to-n as the radius is increased.[9] For a given size, the capping ligands, through their dipoles can also be used to control the majority carrier nature, as pointed out by Chu et al.[88] It has also been evidenced that p- and n- character can be controlled by making the CQD surface respectively anion or cation rich.[15,89]

2.2. Infrared Emission and Carrier Dynamics

The achievements in PL intensity enhancement and wavelength range expansion further into the IR have been closely tied to the development of the synthetic protocols, post-treatment techniques or the emergence of novel nanostructures, such as NPLs or NRs. These synthetic improvements have enabled an excellent control over the size, shape, and spectral tunability of the HgTe CQDs. Early works in the field of HgTe CQDs were focused on the development of the PL properties arising from the $1S_h$ to $1S_e$ interband transition. A. Rogach et al.[90] synthesized water soluble 3 nm diameter HgTe CQDs with a PL band in the SWIR region. Improvements of that synthetic technique allowed the growth of particles up to 6 nm and expanded the emission range up to 2 µm, with the CQDs being transferred to D_2O to reduce OH-absorption (**Figure 3a**).[90] To further expand the range of applications and mitigate the OH-group's parasitic absorption, the water-based synthesis was later transferred to organic solvents, while retaining the PL properties of the material.[91] M. Kovalenko and co-authors[25] significantly improved an aqueous synthesis procedure to obtain narrow size distribution, and the emission band maximum was shifted up to 4 µm. In the same work, a phenomenological equation connecting the CQD size with the PL band maximum position was introduced for this size range. Later on, this synthetic protocol was implemented for the synthesis of HgTe CQDs in aprotic solvents, dimethyl formamide (DMF), which allowed to shift the PL band to 3 µm (Figure 3b).[92,93] Although control of the reaction kinetics, and therefore the size distribution remained challenging when growing large CQDs, this method allows the routine production of sufficient material volume for device applications.

Organic non-polar synthetic approaches were also explored. Following prior work on the synthesis of PbSe CQDs, starting from metal halides and using alkylamines as a solvent, a robust HgTe CQDs synthesis route was developed by controlling the $HgCl_2$ concentration and using TOPTe as the anion source. The absorption and PL ranges were extended up to 5 µm, which was achieved by tuning the temperature and growth time (Figure 1c).[26] In addition, the absorption spectra showed better-defined excitonic features and higher order transitions than previously demonstrated. The products were typically moderately "aggregated" showing a branched structure when imaged under the TEM. Later work explored more reactive telluride sources and found that the commercial bis-trismethylsilyl telluride led to non-aggregated quasi-spherical dots, and this was explained by a surface enriched in mercury. This reaction protocol also led to partial n-doping of the dots, leading to the observation of intraband transitions from the $1S_e$ and $1P_e$ states.[59] The use of highly reactive bis(trismethylsilyl)telluride provided an advantage over other tellurium sources, enabling the production of well-dispersed spherical shapes HgTe CQDs without the need for thiol ligand capping. Their thiol-free surface allowed for successful subsequent modifications and a doping of one or more electrons per dot.

Intraband luminescence in the MWIR is expected in steady state with n-doped CQDs since the $1S_e$ level is partially filled, contrary to undoped CQDs which would need strong excitation to initially populate it. The n-doping of HgTe CQDs and the observation of intraband PL followed earlier reports of intraband PL with HgS[89,94] and HgSe.[95]

To date, the highest MWIR PL quantum yield (PLQY) of mercury chalcogenide cores using interband transitions is $\approx 10^{-2}$–10^{-1}% which is very low. The present record MWIR PLQY of CQDs in solution is obtained with the 5 µm intraband transition of HgSe cores surrounded by thick CdS shells[95] and it is still only ≈2% (Figure 3d).[96] PLQY has been highlighted as the single property fundamentally limiting the ratio of signal to thermal noise for detectors, the specific detectivity scaling with the square root of the PLQY.[97] As a result, improving the PLQY will also have vast benefits for both light emitting devices and photodetectors.

Another direction emerged following the work by the group of S. Ithurria,[8] which reported HgTe NPLs derived from CdTe NPLs through cation exchange. The strong quantum confinement in the HgTe NPLs led to a significant reduction in the full width at half maximum (FWHM) of the band-edge PL (Figure 3e). Subsequent efforts have been made to enhance spectral properties of those materials.[49,81] Notably, the formation of heterostructures comprising dots-on-NPLs (based on HgX, where X is Se or Te) has enabled the achievement of bright and tunable emission through both interband and intraband relaxation.[49] The PLQY has been boosted from 10% to 30% and remained stable even after several months of storage.

As mentioned above, HgTe NRs were synthesized via a two-step cation exchange process.[31] It was demonstrated that by

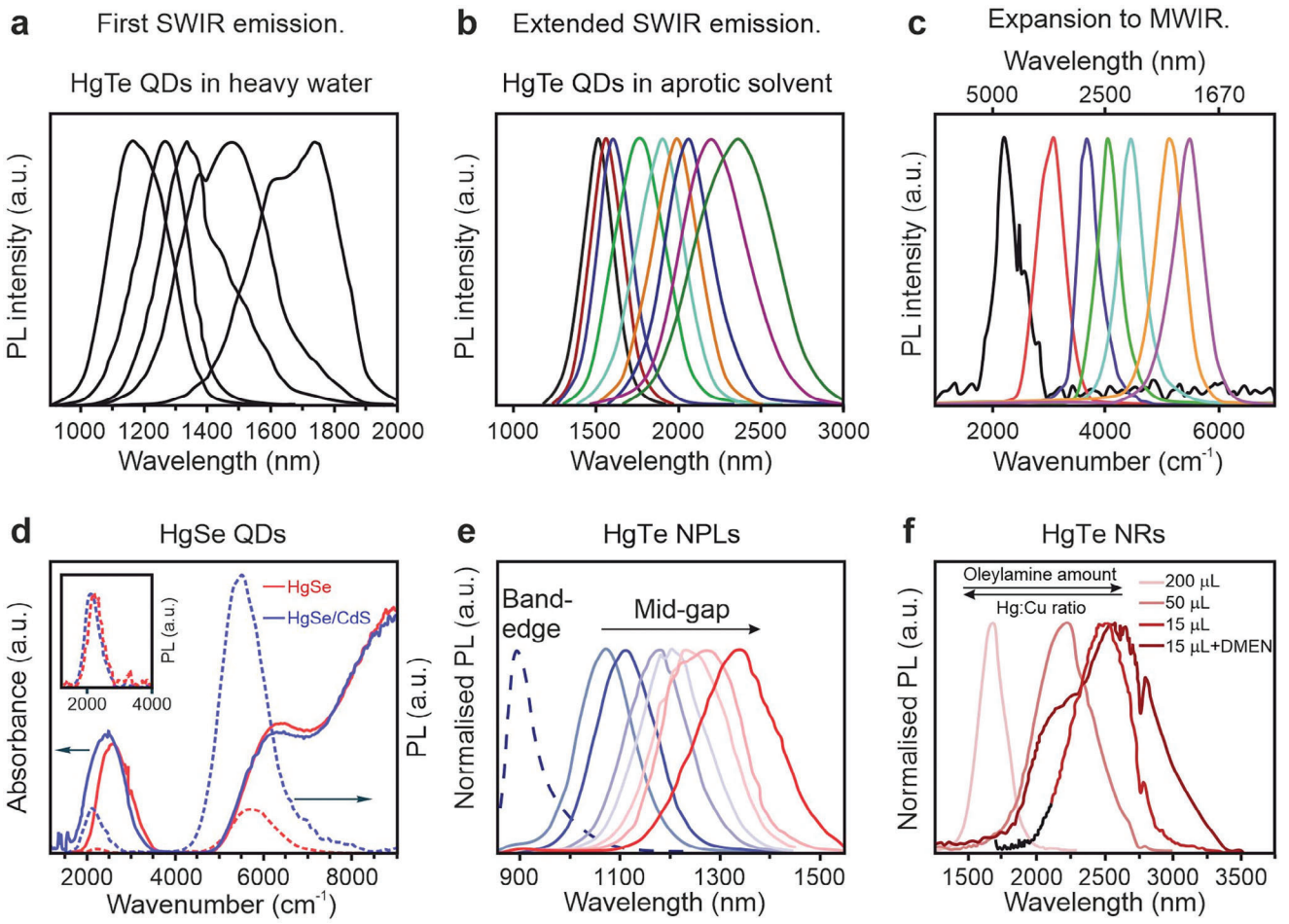

Figure 3. Evolution of the IR emission of mercury chalcogenide CQDs: a) PL of HgTe CQDs grown in H_2O and transferred to D_2O to reduce the OH-group's impact on the emission efficiency. Adapted with permission from,[90] copyright 2001; b) The shift of the PL band of HgTe CQDs synthesized in DMF. Adapted with permission from,[93] copyright 2020; c) PL of HgTe CQDs obtained by hot-injection in non-polar media. Adapted with permission from,[26] copyright 2011; d) Intraband absorption and PL of HgSe CQDs and HgSe/CdS core-shell CQDs. Adapted with permission from,[96] copyright 2021; e) Interband and intraband PL spectra of HgTe heterostructures (dots-on-NPL) with time (up to 75 days aging). Adapted with permission from,[49] copyright 2020; f) Shift of the PL band maximum depending on surfactant amount and Cu content in HgTe NRs obtained by sequential ion exchange steps. Adapted with permission from,[31] copyright 2023.

maintaining a core diameter of 3 nm while extending the length of the NRs to 40 nm, their PL maximum could be shifted to 2.5 µm (Figure 3f). The energy and FWHM of the PL band depended on various factors, including the quantity of surface passivation agents (TOP or oleylamine) and the resulting Hg-to-Cu content. Moreover, due to the strong preference for NR growth along the (002) crystal axis, this material has garnered interest as a potential polarization selective emitter/ polarization sensitive detector.

In the near-infrared region, the PLQY of band-to-band recombination in HgTe CQDs dissolved in aqueous media reached 40% (**Figure 4**). However, the emission efficiency was reduced by resonant energy transfers to solvent and ligand molecules, as illustrated in Figure 4, and to a greater extent, by non-resonant carrier recombinations in HgTe CQDs.[98] The latter refers to the relaxation of an excited charge carrier through polaron energy levels formed by the strong interaction between QD surface trap states and vibrational modes of the surrounding media. By removing these IR overtone and water vibrational modes from the relevant spectral range through solvent replacement of water by organic solvents, the nonradiative lifetime was extended, resulting in a PLQY increase of up to 75% at 1.4 µm for the HgTe CQDs in non-polar media (Figure 4).[71] However, upon moving further into SWIR, the PLQY still gradually decreased to 20% at 2 µm.[92] In the wavelength range between 2 and 5 µm, the resonant energy transfer between HgTe QDs and ligand vibrational bands is a dominant energy dissipation process (Figure 4).[99] To maintain colloidal stability and ensure sufficient interparticle distance, CQDs need to be capped with long-chain ligands, usually consisting of an alkyl tail and a thiol group to bond with mercury ion sites. However, these long alkyl chain ligands exhibit strong IR absorption at ≈3000 cm^{-1},[100] attributed to the resonance modes of C-H bonds. Consequently, the PL efficiency dramatically drops by orders of magnitude.

Auger recombination also affects PL efficiency across the entire IR spectral range except at low fluences where only single exciton occupancy prevails. In this process, excitons recombine non-radiatively by transferring the excitation energy to a third

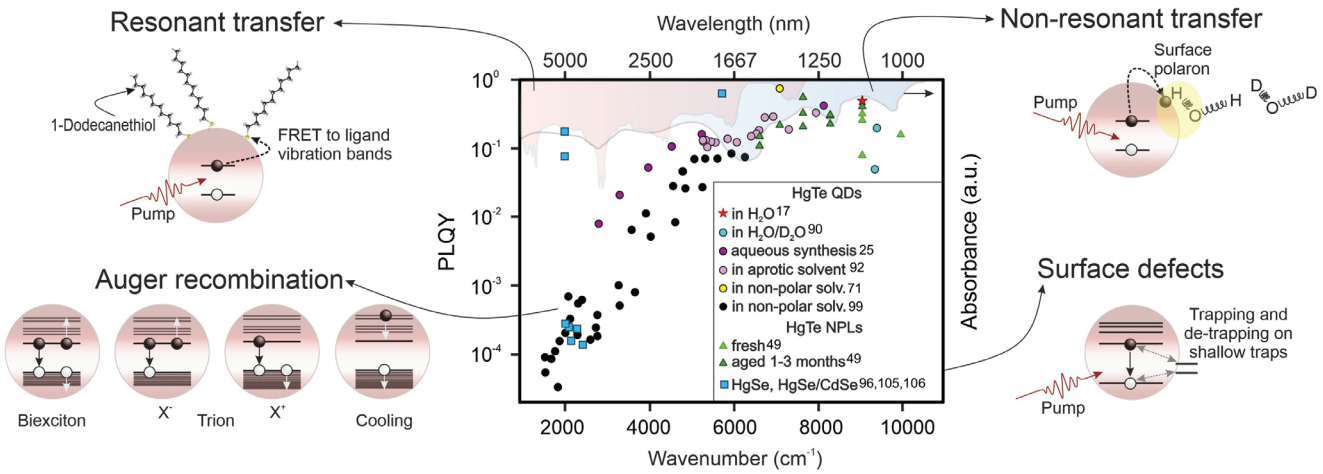

Figure 4. PLQY of HgTe CQDs and NPLs reported in literature (middle graph), and the main channels of the photogenerated charge carriers' energy dissipation, such as resonant and non-resonant transfer, trapping on surface defects, and different kinds of Auger recombination. Red and blue stripes represent the locations of the strongest resonant bands of C-H and O-H groups, respectively, that commonly occur in ligands, solvents and other matrices for CQDs.

body, which dissipates the energy to the CQD lattice through thermalization or phonon recombination.[101] Moreover, reducing the interparticle distance for narrow gap CQD leads to the decreased energy barrier for Auger process, makes it a dominant nonradiative relaxation path. Biexciton and trion Auger recombinations are the most common processes described for SWIR and MWIR emitting HgTe CQDs and their visible range counterparts.[102–104] Stronger quantum confinement can lead to slower Auger process than in the bulk material, and even its suppression in HgS CQDs,[89] and HgSe/CdSe[105] core-shell structures. With thick shells, intraband and interband PLQY can be boosted, in solution, up to 2% at 5 µm and above 50% at 1.7 µm.[96,106]

In isolated CQDs, the low MWIR PLQY is primarily assigned to electronic to vibration energy transfer. The near field coupling is particularly efficient when the band-edge is matched with the energy of the C—H bond resonance at ≈2900 cm^{-1}. This process is nevertheless not limited to the C-H resonance, and similar energy transfers are involved for all resonances relative to the ligand molecules. In this sense, surface passivation is particularly challenging in the mid infrared range. This motivates the attempt to replace conventional organic ligands by inorganic matrices, in addition to seeking a possible increase of carrier mobility. This needs to be conducted in a careful way since incomplete passivation may also result in trap state formation. Time-resolved photocurrent measurement allows to probe both the initial carrier density relaxation and trapping and de-trapping processes.[107] In particular, the estimation of the trap density for different ligands attached to the HgTe CQD surface showed that the shortest ionic ligand (such as S^{2-}) although promising from a charge carrier transport standpoint, tends to introduce a large number of traps. On the other hand, short thiols (such as ethanedithiol[107] or 2-furanmethanthiol)[108] bring the best surface trap passivation, and these conclusions are matched by steady state photocurrent measurements.

In addition to non-radiative recombination processes becoming faster at longer wavelengths, the radiative rate slows down. This means that relaxation by all of the faster non-radiative processes progressively squeezes out the radiative recombination. Thus, it becomes highly desirable to redress or at least partially mitigate the imbalance of radiative and non-radiative rates back in favor of the former.

Different approaches were used in order to accelerate the radiative recombination rate and enhance the PL efficiency of HgTe CQDs. While particle shape altering, ligand-assisted surface chemistry engineering, and the use of core-shell morphologies showed promising results in the MWIR range,[96,106] there is still plenty of room for improvement. In this regard, inspiration might come from a different avenue, *i.e.*, a coupling of narrow band gap CQDs with plasmonic structures. In this case, the Purcell effect would ensure faster radiative rates of the emitters and therefore the emission efficiency roll-off in the IR arising from Fermi's Golden Rule can be partly counteracted.

A. Sergeev et al. demonstrated the possibility to shape and enhance the PL of HgTe CQDs via coupling with a laser printed 3D array of plasmonic nanoantennas in a wide spectral range from 1 to 2.5 µm (**Figure 5a**).[47] Along with up to 5-fold enhancement of the PL intensity, matching the lattice resonance of the plasmonic array with a vibration band of the stabilizing ligand reduced the influence of the QD-to-ligand resonant transfer. This study was further expanded by confirming that this plasmonic metasurface supports bound states in the continuum.[48] Coupling of the HgTe CQD PL band to high quality factor modes of the metasurface improved emission directivity and facilitated a 12-fold enhancement of the PL intensity in the 0.9–1.7 µm range (Figure 5b,c). Despite this high enhancement factor, the implementing of this plasmonic array into LED structures appears challenging. In this case, a simple plasmonic grating may become a more manufacturable alternative. With a right choice of plasmonic grating period the PL intensity of the HgTe CQDs at 1.3 µm can be enhanced up to 2-fold and directed perpendicular to the substrate.[109] Slightly less enhancement coefficient of 1.5-fold was found when the plasmonic grating was covered with HgTe NPLs (Figure 5d,e).[81] Taking into account emission

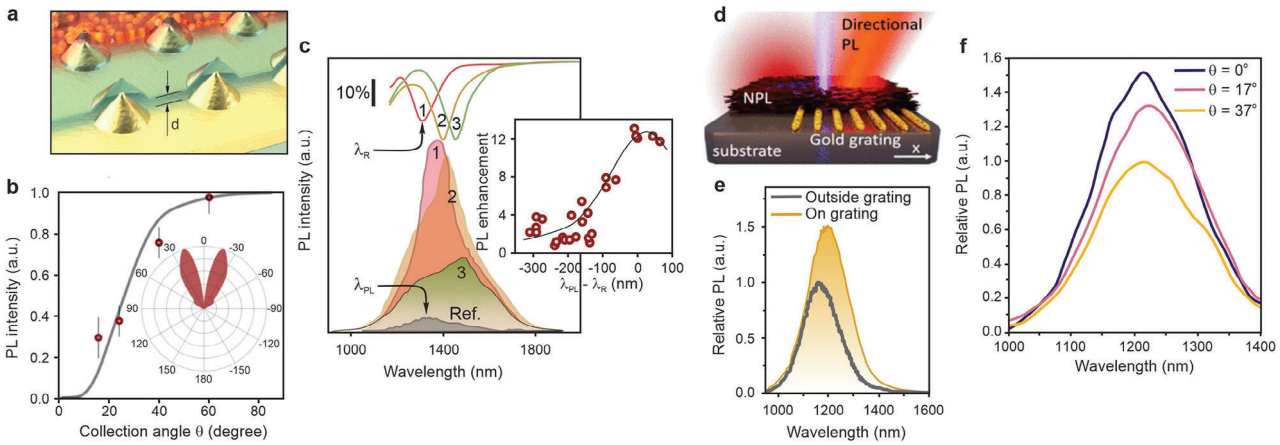

Figure 5. Enhancement of PL of HgTe CQDs via coupling with plasmonic structures: a) A sketch of the Au nanobump array covered with an Al_2O_3 spacer layer of thickness, d (green), and HgTe CQDs (in red); b) Directivity of the PL from the HgTe CQD film; c) Shaping and enhancement of the HgTe CQD PL profile depending on the position of the plasmon resonance (the insert shows the PL enhancement versus the offset); a–c) Adapted with permission from,[48] copyright 2023 d) A sketch of an Au grating combined with a layer of HgTe NPLs to effect emission enhancement; e) Relative PL intensity of HgTe NPLs outside and within the footprint of the grating; f) Directivity of the PL of the HgTe NPLs while collecting the light though a 10X microscope objective. d–f) Adapted with permission from,[81] copyright 2023.

directivity control (Figure 5f), this approach appears promising for real device design. However, several questions are still to be solved here, such as modeling of the complex index of all the layers in the stack, and tailoring the device structure architecture with proper (optimal) consideration of the grating parameters.

Nevertheless, significant advancements in emission efficiency enhancement and understanding of the charge carrier dynamics have facilitated the development of LEDs based on mercury chalcogenide CQDs. In the earlier study, D. Koktysh et al.[20] demonstrated NIR electroluminescence (EL) from HgTe CQDs embedded in a conducting polymer matrix (**Figure 6**a,b). The EL exhibited a maximum at 1.3 µm, closely matching the PL spectrum. Although the turn-on voltage for detectable NIR light emission was relatively high (≈10 V), a strong brightening of the EL

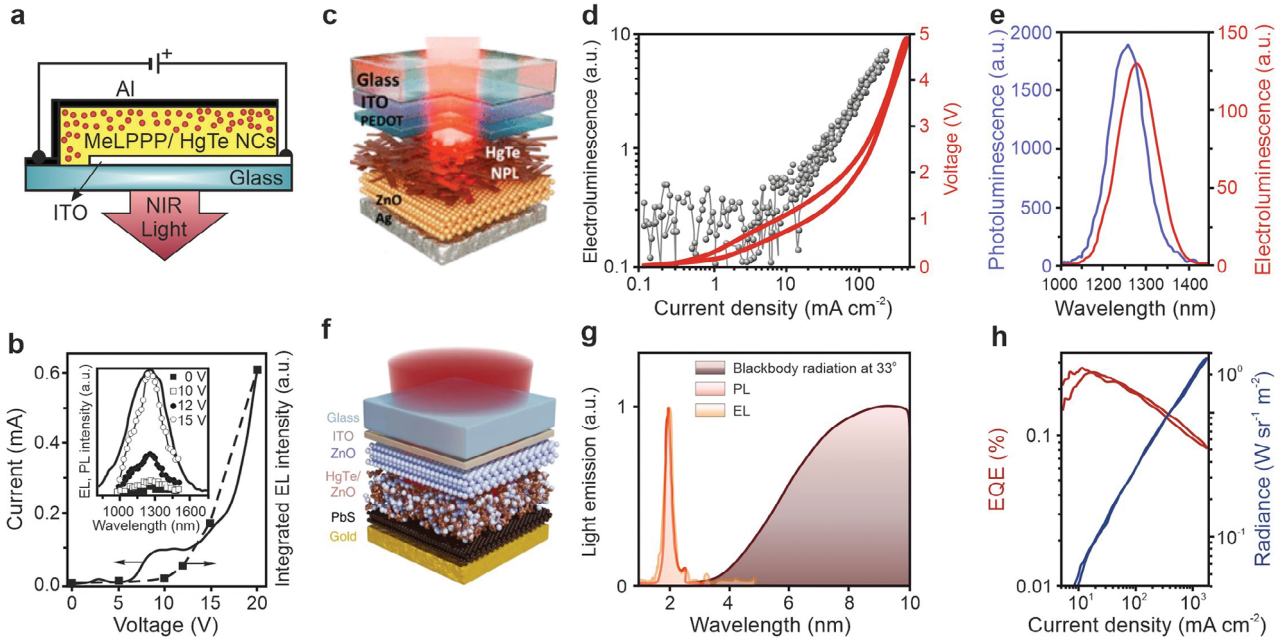

Figure 6. Electroluminescence of HgTe CQDs. a) A sketch of the first reported LED based on HgTe CQDs embedded in a conducting polymer matrix; b) Dependence of the current and EL intensity under applied bias. The inset shows EL spectra of HgTe CQDs-polymer LED under different bias levels; a,b) adapted with permission from,[20] copyright 2004. c) Design of the HgTe NPL based LED emitting at 1.3 µm; d) EL intensity and I-V characteristics of the HgTe NPL LED; e) PL and EL spectra of the HgTe NPL LED. f–h) Adapted with permission from,[81] copyright 2023. f) Design of a HgTe CQDs-based LED emitting at 2 µm; g) PL, EL and 33 °C black body spectra of the HgTe CQDs-based LED; h) Dependence of the EQE on current density. c–e) Adapted with permission from,[41] copyright 2022.

band was observed with increasing applied voltages. It was found that charge carrier transport in the polymer-HgTe film was limited by trap states. Additionally, the energy level offset between the CQDs and the polymer matrix hindered charge carrier injection under forward and reverse bias. Due to these limitations, along with morphological changes in the film during operation, the external quantum efficiency (EQE) of the NIR emission was estimated to be only 0.001%. Soon after, a second example based on PEDOT:HgTe CQDs junction[19] showed similar modest efficiency, but it is worth noting that despite being low, those values were comparable to the reported EQE of PbS CQD-based LEDs at that time.

It took more than a decade (from 2004 to 2020) and significant improvements in CQD synthetic techniques and device engineering before the next reports on HgTe CQD EL emerged.[30,71] Recent reports showed that HgTe NPLs can be bright emitters.[81] The diode structures based on these NPLs presented a narrow EL band overlapping with the PL band at 1.3 µm and a bias threshold at 0.9 V (Figure 6c–e). Taking inspiration from PbS-based LED,[110] design of LED[41] with emission above 2 µm has been proposed. The active material made of HgTe CQDs was placed between ZnO and PbS as electron and hole injectors, respectively (Figure 6c). Furthermore, HgTe CQDs were mixed with ZnO to achieve better charge balance through HgTe doping. The device exhibited a low turn-on voltage of 0.6 V, matching the HgTe CQDs bandgap, and an operational lifetime of up to 10 h. It was observed that the EQE is strongly depended on the ZnO content in the HgTe mixture, ranging from 0.1% to 0.3% (Figure 6d,e). These values correlated well with the PLQY of the mercury chalcogenide in the SWIR range (2–2.3 µm).

The EL of the reported HgTe CQD-based LEDs arises from the interband transition, and therefore its internal efficiency cannot exceed that of the PL. However, emission through intraband transitions offers advantages such as a small mid-gap energy, the potential for a reduced laser threshold, and slowed Auger recombination rate. In this context, EL at 5 µm was demonstrated from core-shell HgSe-CdSe CQDs sandwiched between ZnO and polyvinylcarbazole electron and hole transport layers, respectively.[51] It was observed that the EL occurred via cascade tunneling of injected carriers from the $1S_e$ state of one quantum dot to the $1P_e$ state of another one, with some radiative relaxation occurring at each step. The highest EQE and power conversion efficiency (PCE) of the device reached 4.5% and 0.07%, respectively, under a current density of 2 A cm^{-2}. Remarkably, the intraband EL efficiency was 60 times higher than the estimated PLQY (0.075%) of the same intraband transition, due to the cascade effect.

3. Theory and Electronic Structure Modelling

HgTe is a material, particularly known for its peculiar band structure at the origin of its interesting properties and applications. In its low-pressure phase, it crystallizes in the ZB structure[111–113] typical of III-V and II-VI semiconductors. In this form, it is characterized by the absence of an energy gap between conduction and valence bands, see **Figure** 7a. The semi-metallic character of HgTe is well accepted,[114–117] whereas it was more debated in the case of HgSe[118–121] and especially HgS because of excess doping and the unstability of bulk HgS in the small gap ZB structure.[117,122,123]

The key aspect of bulk HgTe is its inverted band structure at the Γ point (the center of the Brillouin zone, $k = 0$). In a typical semiconductor like CdTe (Figure 7b), the s-like Γ_6 band forms the conduction band, and the p-like Γ_8 and Γ_7 bands form the valence band. Γ_8 ($p_{3/2}$ bands) and Γ_7 ($p_{1/2}$ bands) are split by spin-orbit interaction, the top of the valence band is Γ_8. The energy gap E_g, taken as the energy difference between Γ_6 and Γ_8, is therefore positive. On the contrary, in HgTe, Γ_6 and Γ_8 bands are inverted (Figure 7a), as a result of the high atomic number of Hg that leads in particular to large splitting of 5d states by spin-orbit coupling and to 6s states particularly low in energy.[126,127] For this reason, HgTe is often considered as a negative-gap material, which is not just a figure of speech, as we will see below. Commonly accepted values of E_g for HgTe are of the order of −0.30 eV at 0 K,[114,116] with an important dependence on temperature[116,128] ($E_g(T) \approx E_g(0) + 6.3 \times 10^{-4} T^2/(11 + T)$) leading to $E_g \approx -0.12$ eV at 300 K. However, it is important to realize that, as long as E_g is negative, the highest occupied states and the lowest unoccupied states are all of Γ_8 character and touch at $k = 0$, i.e., the energy gap between them is vanishing (Figure 7a).

A transition to the normal band order (*i.e.* $E_g > 0$) can be approached by applying hydrostatic pressure following the relation $d E_g = 3\alpha\, da/a$ where a is the lattice parameter, the deformation potential α and the compressive strain da/a being both negative. Measurements on HgTe/HgCdTe superlattices yielded $\alpha = -3.69$ eV,[129] while a smaller value of −2.4 eV was obtained in HgTe nanocrystals.[111] However, HgTe transforms into other crystalline phases at high pressure.[111–113,130]

The Γ_8 conduction and Γ_6 valence bands of HgTe are characterized by very low effective masses ($\approx 0.01 m_0$ where m_0 is the free electron mass), but their energy dispersion rapidly becomes almost linear as k moves away from zero[124,131] as they are mutually coupled by the $k.p$ interaction.[115] For the same reason, even though the Γ_6 valence band has a pure s character at Γ, its weight on s orbitals strongly and quickly decreases with increasing $|k|$ (Figure 7a). The opposite behavior is found for the Γ_8 conduction band.

Modelling the properties of HgTe therefore requires an excellent description of its band structure. This proves difficult, even with the most elaborate ab initio calculations. Indeed, it is necessary to simultaneously consider spin-orbit coupling and many-body effects beyond the (semi-)local approximations of density functional theory.[126,127,132] The $k.p$ theory is therefore still widely used to describe HgTe and its nanostructures, as it is specifically parameterized to accurately describe bands in the vicinity of the Γ point. Numerous parameter sets are available in the literature.[113,131,133–135] More elaborate semi-empirical methods describing the band structure across the entire Brillouin zone, such as empirical pseudopotentials[111,136–139] and tight-binding,[124,140] have been developed for HgTe. The most recent models offer a description of the electronic structure of bulk HgTe in close agreement with ab initio calculations and experimental data, ensuring good transferability to nanostructure studies.[124,138,141]

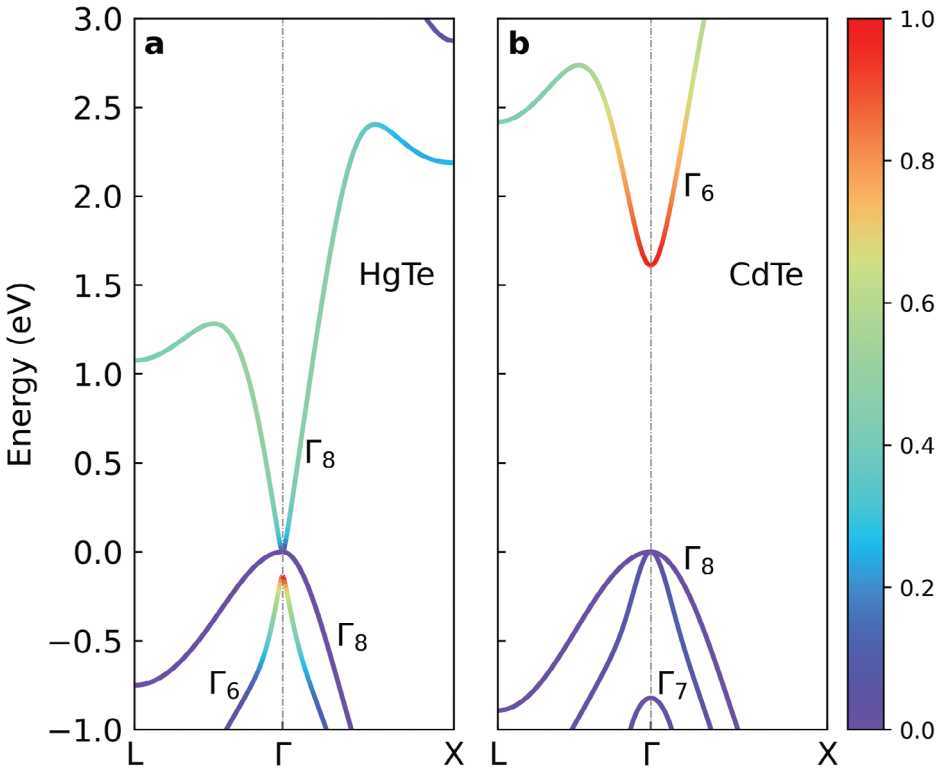

Figure 7. Electronic band structures of HgTe (a) and CdTe (b) calculated with tight-binding modelling using the parameters of[124] and,[125] respectively (zero of energy = top of the valence band). The color of the lines indicates the weight of the Γ_6 states on s atomic orbitals normalized to unity.

3.1. Bandgap Engineering

The inversion of Γ_6 and Γ_8 bands is responsible not only for the semi-metallic character of bulk HgTe, but also for its exceptional opto-electronic and topological properties which, however, require opening an energy gap in the band structure. To achieve this, a well-known approach for many years has been to consider the mixed compounds CdTe-HgTe.[142] Remarkably, the energy gap of the $Hg_{1-x}Cd_xTe$ alloy varies as a function of Cd composition x over almost 2 eV, from 1.6 eV for CdTe down to −0.3 eV for HgTe and therefore spans the entire infrared spectrum.[134,143] This explains why $Hg_{1-x}Cd_xTe$ is a material of choice for detection in the various IR ranges.[4] In this approach, gap opening only occurs when normal band order is restored, i.e., when $E_g > 0$.

The other approach of interest here is quantum confinement, which, unlike the previous case, can open a gap in the band structure even when the Γ_6-Γ_8 order remains reversed. The material formed is then a topological insulator which, at the boundaries with a normal insulator, is characterized by conducting edge or surface electronic states that are topologically protected.[144] Thus, it has been shown that HgTe quantum wells with thickness d_w greater than ≈ 6.3 nm are 2D topological insulators exhibiting a quantum spin Hall state.[5,145] For $d_w \lesssim$ 6.3 nm, quantum confinement is such that the normal Γ_6-Γ_8 order is restored, returning to the situation of a normal insulator as in usual III-V or II-VI semiconductor quantum wells. A 3D topological phase can be also obtained in thick HgTe films under strain induced by the lattice mismatch when deposited on CdTe.[146,147] Devices exploiting the quantum spin Hall effect or the unique transport properties due to the inverted band could lead to new kinds of transistors, sensors, and quantum information devices. But the main application of quantum confinement in HgTe/HgCdTe quantum wells remains infrared photodetectors. These devices are designed to have discrete energy levels (mini-bands) that correspond to specific IR wavelengths, making them highly effective for wavelength-specific detection.[4,148]

In HgTe CQDs, the effect of quantum confinement is much stronger than in quantum wells, since it applies in all spatial directions. Several *k.p* calculations of their electronic structure have been published, with various levels of approximation.[7,36,56,149–152] Investigations of the few-electron ground state in topological HgTe CQDs can be found in ref. [152]. The *k.p* calculations of ref. [56] predict optical gaps and cross sections in good agreement with experiments. This work was subsequently supplemented by atomistic tight-binding calculations, which are summarized below.

Figure 8 shows that the energy gap between occupied and empty states of HgTe CQDs can vary over a wide energy range, from zero in the bulk limit to over 0.8 eV for diameters d below 4 nm. The QD gap varies as $1/d$ and not as $1/d^2$ as predicted by the well-known particle-in-a-box model.[141] This is due to the linear dispersion of the bands as a function of k when moving away from the Γ point as previously discussed.[6] Remarkably, the linear variation of the energy of the gap edge states (Figure 8a) extrapolated to $1/d \to 0$ gives a negative gap of −0.15 eV, close to the Γ_6-Γ_8 gap of −0.14 eV predicted by the tight-binding model at 300 K.[124] This confirms that describing HgTe as a negative-gap

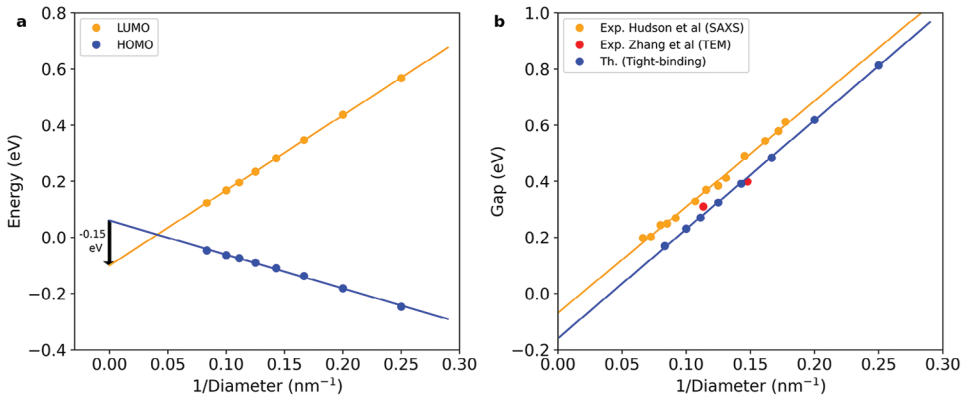

Figure 8. Band gap simulation and sizing curve for HgTe CQDs. a) Energy of the highest-occupied (blue) and lowest-unoccupied (orange) states calculated in tight-binding[124] as function of inverse diameter of spherical HgTe QDs. b) Evolution of the bandgap compared to experimental data (Hudson et al.[153] and Zhang et al.).[67] Lines are linear interpolations and extrapolations; the calculated gap varies like $E_g = -0.15 + 3.83/d$ with E_g in eV and d in nm. Adapted with permission from ref. [6].

material has some physical reality. This finding is supported by plotting experimental data from refs. [6,153] (Figure 8b). The topological transition (between normal and inverted Γ_6-Γ_8 order) is estimated for a diameter of the order of 26 nm, although this value deserves further calculations specifically dedicated to this size range. This same transition has been studied theoretically in the case of HgS CQDs in ref. [154].

As already shown for other semiconductor compounds,[141] the band gap of CQDs with cubic, tetrahedral, truncated tetrahedral, or octahedral shape is very close to the band gap of spherical CQDs with the same volume.[6,62,63,124] As expected, there are more discrepancies for shapes that differ most from spheres, such as tripods, or rods with large length-to-width ratio. However, atomistic methods enable the electronic structure to be calculated directly from knowledge of the complex shape of a CQD, for example deduced from electron tomography measurements.[63]

Figure 9a shows a typical example of an electronic state spectrum calculated in tight-binding for a truncated tetrahedral HgTe CQD with an average diameter of 6.3 nm. The lowest-energy unoccupied state ($1S_e$), doubly degenerate due to spin (Figure 9b), is characterized by a wave function whose envelope is close to a 1S orbital obtained in a spherically symmetric potential well.[141] The next unoccupied level ($1P_e$), made of a manifold of six states, can be associated with a 1P state. The density of occupied states is much higher than that of unoccupied states. The highest-energy states are denoted $1S_h$ and $1P_h$ rather by convention, as their wave functions turn out to be rather complex, even their respective order depends on the size (Supporting Information of ref. [27]). This complexity arises from the very particular band structure of HgTe, the nature of its electronic states and couplings, which are highly k-dependent. It should be noted that this CQD, like most HgTe CQDs obtained by colloidal synthesis, has dimension below 26 nm, and is therefore in the normal insulator state. This is reflected in the fact that the lowest-energy unoccupied state ($1S_e$) is characterized by a strong component on the s atomic orbitals (of the order of 70%), whereas this component is virtually zero for the highest-energy occupied state.[6] This is the usual situation for CQDs in conventional III-V or II-VI semiconductors. However, as CQDs increase in size and approach the

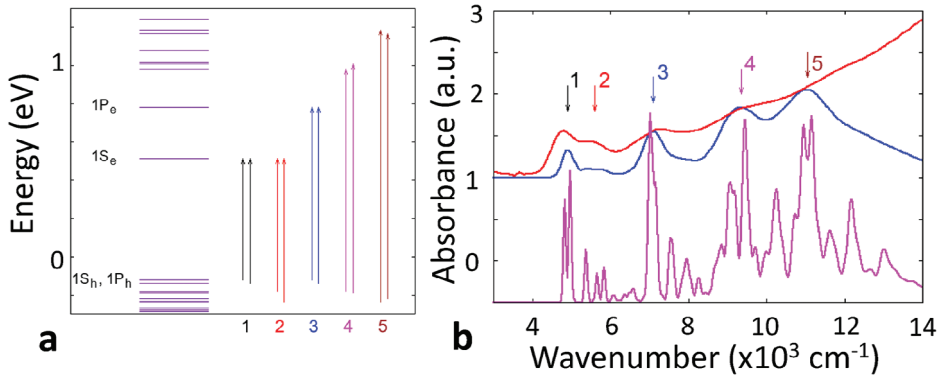

Figure 9. Modelling optical spectra of HgTe CQDs: a) Energy levels calculated for a 6.3-nm diameter HgTe CQD of truncated tetrahedral shape. Zero energy corresponds to the Fermi level in bulk. Arrows: assignment of the main absorption peaks. b) Comparison between calculated (purple/blue lines) and measured (blue line) absorption spectra. Each transition line of the calculated spectrum is broadened by a Lorentzian function purple curve: broadening of 4 meV; blue curve: broadening increasing linearly with energy from 15 meV at 4000 cm^{-1} to 65 meV at 12 000 cm^{-1}). The size of the CQD is chosen so that the position of the lowest-energy absorption peak agrees with experiments. Adapted with permission from ref. [27].

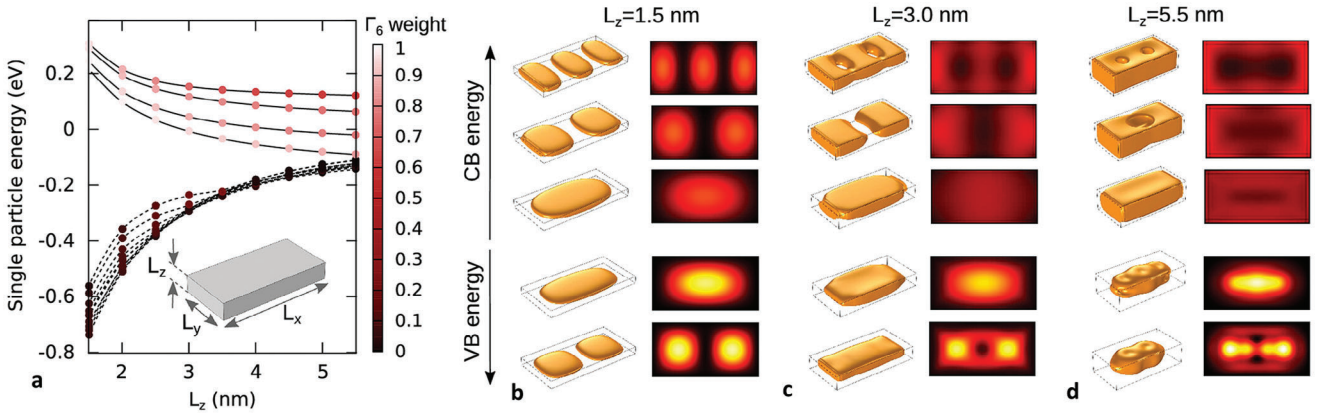

Figure 10. Electronic structure of single-particle states of HgTe NPLs as a function of their thickness. a) Energy levels around the band gap. Dots are calculated points, solid (dashed) lines are guides to the eye for the conduction (valence) band. The dot color indicates the weight of the Γ_6 band in the state. The origin of energies is set to the top of the Γ_8 band in bulk HgTe. The inset shows the geometry of the nanoplatelet under study. b–d) Evolution of the charge density of the three lowest conduction (two highest valence) states, as a function of the nanoplatelet thickness. The iso-surfaces contain 90% of the density. Surface planes are plotted on the x-y plane, at half height. In all cases, the nanoplatelet has lateral dimensions (L_x, L_y) = (20, 10) nm. Conduction states evolve gradually toward edge states. Reproduced from ref. [7].

topological transition, the $1S_e$ state gradually localizes on the surface (see Supporting Information of ref. [27] for HgTe CQDs, ref. [154] for HgS CQDs). Such a transition from a bulk state to a surface (edge) state has also been predicted in the case of HgTe NPLs (**Figure 10**).[7] Finally, as HgTe CQDs can be seen as artificial atoms with very strong spin-orbit coupling, their self-assembly to form a 2D honeycomb lattice could result in a material with quite remarkable topological properties, if disorder effects can be minimized.[155]

Strong quantum confinement moves the conduction states further away in energy from the valence states. This tends to freeze the effects of spin-orbit coupling in the $1S_e$ conduction state, resulting in a gyromagnetic factor g approaching the value of the free electron ($g_0 = 2$) for the smallest sizes.[156] Thus, g is predicted to vary from −19.34 to +1.37 for sizes ranging from 20 to 4 nm.[150] Such huge variations are also found in CQDs of small-gap semiconductors such as InAs or InSb.[156]

3.2. Optical Properties

Due to the low effective electron mass in HgTe,[113,157] and consequently the large Bohr radius of the exciton, excitonic effects on optical properties are small for CQD sizes of the order of ten nanometers and less.[124,157] Consequently, calculations considering single-particle transitions are justified in this regime of strong quantum confinement.[141] For example, *k.p* calculations estimate oscillator forces at the optical gap in good agreement with measured integrated optical cross sections.[56]

Tight-binding calculations allow to interpret optical absorption spectra considering the many different electronic states. An example is shown in Figure 9b. A significant broadening of the peaks is necessary for good theory-experiment agreement. This shows that each experimental peak is in fact made up of several transitions involving, in particular, several occupied states with a high density of states. The calculations (not shown) qualitatively explain the evolution of absorption spectra as a function of CQD size, despite unavoidable uncertainties about their size and shape.[27]

Figure 11 describes more precisely the size-dependent evolution of the two lowest-energy absorption peaks for spherical HgTe CQDs. These peaks are in fact the result of several transitions as discussed above. The oscillator strength of the second peak increases strongly with size, which is not the case for the first peak, so that both peaks can become indistinguishable at large diameter if the inhomogeneous broadening is large.[6,124] The evolution of the energy position of the two peaks as a function of diameter is in reasonable agreement with the experimental data of refs. [67,153] Quite similar curves of optical gap versus size were deduced from measurements on HgTe CQDs with more tetrahedral shape in ref. [27].

These electronic structure calculations were combined with the use of an effective medium model to calculate the complex optical index of CQD films.[6] They reveal that the complex dielectric constant of isolated CQDs differs considerably from that of bulk HgTe and depends strongly on their size, especially for the real part.

Numerical studies were also used to interpret infrared spectroscopy experiments carried out on n- or p-type CQDs.[36] They confirm that doping induces a bleach of interband transitions and the appearance of new intraband optical transitions.[124] Electron-doped HgTe CQDs show an intra-band peak corresponding to the transition of electrons from the $1S_e$ level to the $1P_e$ level. This peak presents several structures that theory interprets as the lifting of $1P_e$ state degeneracy under the combined effect of spin-orbit coupling and CQD shape anisotropy.[153] This unusually strong spin-orbit coupling results from the high atomic number of Hg and Te.

Recent experiments have demonstrated that HgTe CQDs can exhibit stimulated emission in the telecom IR window characterized by a very low threshold.[158] This behavior is attributed to the presence of surface defects, the system being described by a 4-level model. Ab initio calculations show that a gap state localized on the 5p orbital of a doubly coordinated tellurium atom at the

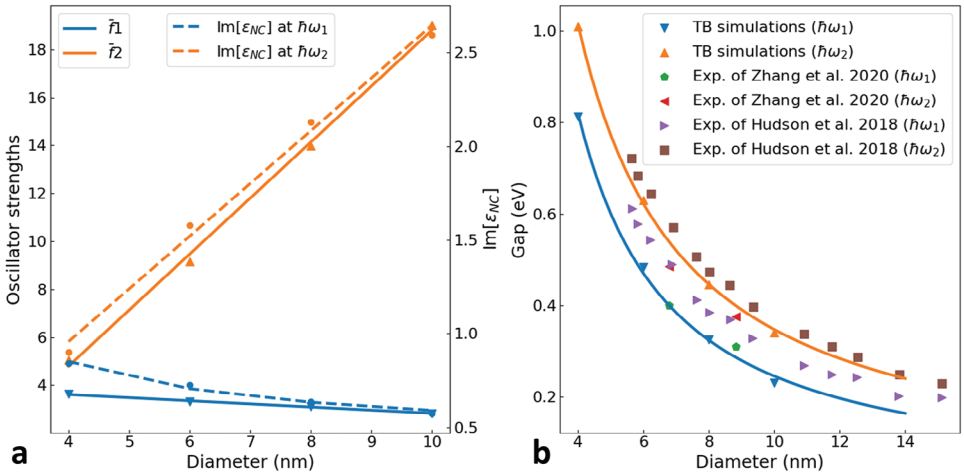

Figure 11. Size-dependent evolution of the two lowest-energy absorption peaks for spherical HgTe CQDs. a) Oscillator strengths $\bar{f}_i$ (solid line), imaginary part of the CQD dielectric constant $Im[\epsilon_{NC}(\omega_i)]$ (dashed line), and b) transition energy $\hbar\omega_i$ for the optical absorption peaks ($i = 1, 2$) versus diameter of spherical HgTe CQDs. Experimental data of H. Zhang et al.[67] and M. Hudson et al.[153] Reproduced from ref. [6].

surface may result from incomplete passivation and explain the stimulated emission. Other interesting properties can be studied from electronic structure calculations of HgTe CQDs, such as the quantum efficiency of multiple exciton generation.[159]

4. Coupling of HgTe CQDs to Light Resonators

Optoelectronic device performance hinges significantly on the interaction between light and matter. In the absence of a photonic cavity, this interaction is dictated by the material itself. Nanoscale dimensions influence the band edge energy through quantum confinement and also impact absorption magnitude via particle packing density. For SWIR and MWIR HgTe CQDs, the absorption coefficient has been found to be a few 10^3 cm^{-1},[56] implying the need for several μm of CQDs film to fully absorb incident light.

Practically, this results in a trade-off in film thickness: while thick absorbing films are desirable to maximize absorption, inefficient charge collection on such films due to limited diffusion length, along with challenges in forming high-quality films above 500–1000 nm, pose constraints. This likely explains why vertical geometry devices[50,160–162] and short-channel planar ones[163] have demonstrated the highest performance. Efforts[164] over recent years have thus been dedicated to coupling infrared-active films with photonic cavities[165,166] to overcome these limitations.

For light detection, the concept aims to trap light within the device to enable multiple passes of the film through the active area, effectively maximizing absorption and reducing the electrically active volume and thus minimizing the noise. Conversely, this concept holds significance for light emission. The index mismatch in a diode ($n = 2$-3 for emitting material, and $n = 1$ for air) makes it challenging to couple emitted photons inside an LED to the far field. As a result, ≈80% of emitted photons are lost, limiting quantum efficiency to 20% and generating heat in the device due to reabsorption, further reducing luminescence efficiency. Hence, efforts to couple HgTe CQDs to photonic cavities have been developed, aiming to boost their PL.[47,48,81,109,167,168]

A diverse range of photonics structures has been coupled to HgTe CQD IR films, which can be broadly categorized into three main types:

1) **Resonators based on single antennas**: These involve subwavelength resonators, such as metallic NRs or bowties, coupled to the HgTe CQDs film (as depicted in **Figure 12a**). This concept is versatile, compatible with both bottom-up approaches (like colloidally grown NRs)[28] and top-down fabrication[170,171] where rods are defined using techniques like e-beam lithography. In the latter case, organizing antennas into a lattice can generate a collective mode similar to a grating.
2) **Fabry-Perot-like cavities**: These cavities involve enclosing the active medium between two reflective interfaces (as shown in Figure 12b).[169] Traditional approaches use metallic mirrors, but the same concept extends to any interface with an index mismatch.[172] Textured substrates (e.g., metal on a dielectric substrate) coupled to CQDs offer interesting advantages, such as the use of flexible substrates to minimize aberrations for wide-angle incident beams compared to normal incidence.[169] It is also a straightforward strategy for transfer to the focal plane array (FPA).[42,45] An extension of this concept is the Bragg mirror,[173] based on dielectric materials, thereby reducing losses in metallic parts.
3) **Grating-based structures**: These structures (illustrated in Figure 12c) use periodic arrangements to diffract non-propagating modes (such as plasmons)[29,174] or propagating modes (like Guided Mode Resonators).[85,175–177] Patterns within a period can incorporate substructures to generate multiple resonances.[178]

Additionally, concepts based on lenses,[179] fiber couplers,[180] or resonators inspired by acoustics[181] have also been explored for specific purposes. Each of these structures offer unique advantages and can be tailored for particular applications and performance enhancements in HgTe CQD films.

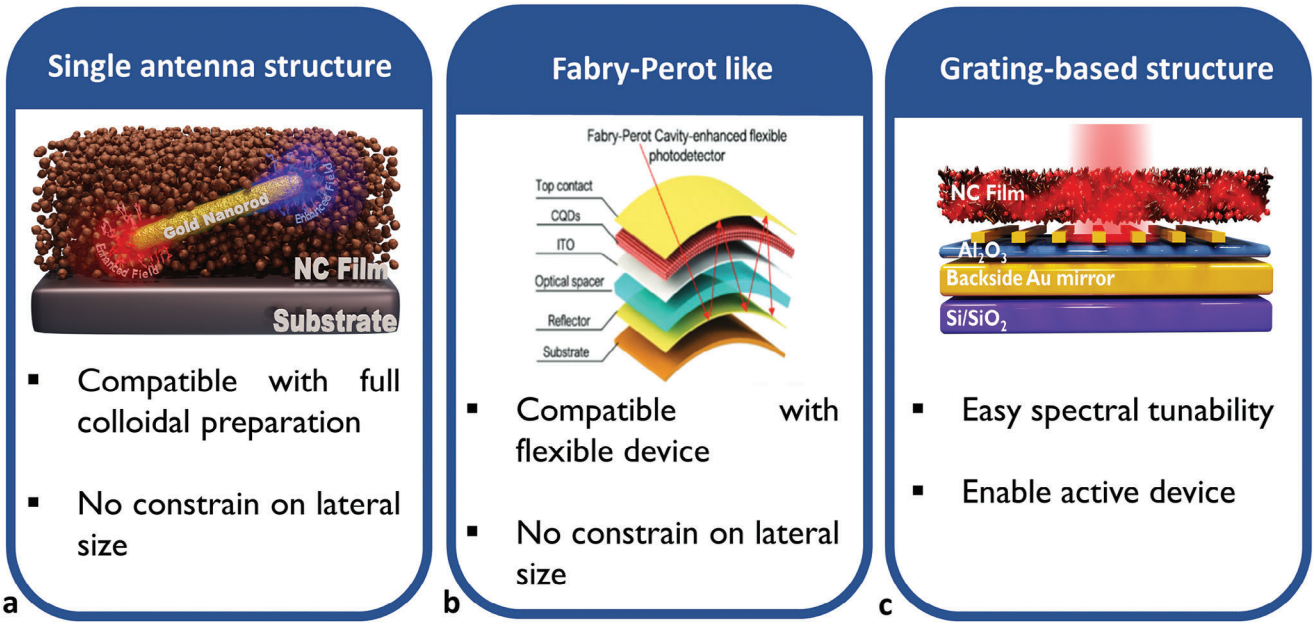

Figure 12. Concepts for light resonators. Schematics of some common methods to generate a light resonance in a nanocrystal film either using resonance from single antenna (a), Fabry-Perot-like cavity (b) or grating based cavity (c). Part b is adapted with permission from ref. [169]. Part c is adapted with permission from ref. [164].

The task of modelling optoelectronic devices based on colloidal CQDs can indeed be quite challenging due to the limited input parameters available. However, when it comes to their optical properties, the key parameter mostly revolves around the complex optical index. Studies by P. Rastogi et al.,[177] later expanded into the mid-infrared range by B. Chehaibou et al.,[6] systematically measured the complex optical index of HgTe CQD thin films as a function of band gap and surface chemistry. Interestingly, they found that using long capping ligands[109] resulted in a low refractive index value ≈2. Shorter ligands, particularly those used for transport purposes (like short thiols[177] or hybrid passivation),[13,14,70] led to higher optical indices in the range of 2.2-2.3. Moreover, it has been noted that the frequency dependence of the refractive index is relatively weak in these materials and can be reasonably neglected in subsequent designs of photonic structures. B. Chehaibou et al.'s work[6] particularly emphasized that the filling factor is likely the primary driving parameter influencing the value of the refractive index in these CQDs.[6]

When designing photonic structures, electromagnetic simulations play a crucial role. However, the initial structure is often conceptualized using basic analytical scaling rules. The primary step is usually to align the cavity's resonant wavelength (λ_r) with the absorption band edge, setting the geometrical factor of the cavity. Early-stage design frequently relies on these analytical scaling rules. For instance, in a Fabry-Perot structure, the thickness of the absorbing layer can be scaled to match $\lambda_r/2n$, while for a plasmonic grating, the period becomes λ_r/n, where n is the refractive index. Aligning the resonance wavelength with the material's band gap leaves several free parameters (e.g., filling factor of the grating, height of the grating, etc.). Determining these parameters is guided by the maximization of effective absorption. It's crucial to note that for generating photocurrent, absorption must occur within the semiconducting nanocrystal layer itself and not within the electrodes or substrate. Therefore, optimization of these structures revolves around maximizing the absorption of incident photons within the active semiconductor layer to enhance device performance.

4.1. Spectral Shaping

The initial drive behind introducing light resonators coupled to HgTe CQD films was to amplify absorption, aiming to focus light on a thin slab with a thickness compatible with efficient charge collection. Reported enhancements in absorption typically range from 3-[164,170] to 10-fold.[181,182] Considering a 200 nm thick film (relatively easy to fabricate and only a few times the diffusion length)[108,183] absorbs roughly 10% of incident light, a ten-fold increase in absorption implies near-complete absorption. However, the increase in photocurrent can often surpass the rise in absorption, especially if the structure supports photoconductive gain. A. Chu et al. showcased a remarkable 1000-fold increase in photocurrent.[164] This achievement stemmed from shrinking the interdigitated electrode spacing to match the criteria of period size to λ_r/n, as defined earlier. Additionally, reducing the period size is advantageous for gain generation because gain is inversely proportional to transit time, meaning that the time for charge to move from one electrode to the other scales with the inter-electrode distance. This reduction in period size not only matches the resonator criteria but also facilitates greater photoconductive gain due to decreased transit time.

4.1.1. From Narrow to Broadband

The advantages of a light resonator extend beyond a simple increase in absorption magnitude, as the bandwidth of this

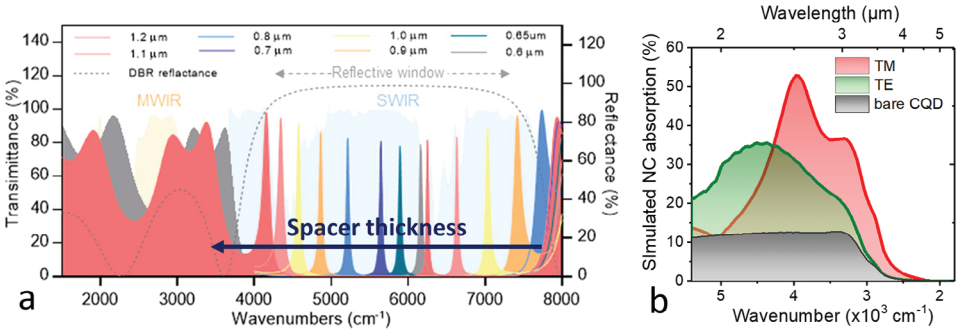

Figure 13. Spectral shaping using a light resonator. a) Absorption spectra of HgTe CQD film coupled to two Bragg mirrors deposited on each side of a spacer the thickness of which is tuned. Part a) is adapted with permission from ref. [173]. b) Photocurrent spectra of a bare HgTe CQDs film and a film with same thickness coupled to a grating that induced three resonances. Part b) is adapted with permission from ref. [172].

enhancement represents another significant degree of freedom. This bandwidth is closely linked to the resonator's technological design and the intended applications. For the sake of illustration, the PL linewidth of HgTe CQDs is typically a bit above 10% of the peak energy and the same order of magnitude holds for the first absorption feature. Through the introduction of a photonic cavity, spectral shaping can be obtained leading to a sharpening or a broadening of the feature. Spectroscopic applications, like gas sensing, aim for narrow spectral lines that align with molecular absorption, while imaging typically targets broadband absorption. In the SWIR and MWIR, the quality factor ($\Delta\lambda/\lambda$) for PL emission usually falls within the range of 5–10.[25,47,99,109] X. Tang et al. demonstrated the use of a doublet of Bragg mirrors, showcasing narrow transmission lines down to 30 cm^{-1}.[173] This roughly corresponds to a 20-30-fold narrowing of the exciton signal, as shown in **Figure 13**a. On the contrary, reports have highlighted broadband enhancements of absorption. In these scenarios, multiple resonators[29,172,184] are coupled to the absorbing layer, some of which may not resonate with the semiconductor band gap. The challenge in combining multiple resonators[185] lies in avoiding an exponential increase in fabrication complexity. T. Dang et al. illustrated that combining a plasmonic grating with vertical Fabry-Perot and a guided mode resonator could be achieved from a single grating structure.[172] This combination resulted in the enhancement of absorption over more than 2000 cm^{-1}, showcasing broad increase in absorption bandwidth, see Figure 13b.

4.1.2. Benefits for Detection

The incorporation of light resonators can offer more advanced benefits beyond immediate increase in absorption and spectral shaping. One such benefit is the reduction of the effective electrical volume. In IR sensors, the competition between photon activation and phonon activation of carrier generation often diminishes the signal-to-noise ratio, resulting in detectivity orders of magnitude lower compared to sensors operating in the visible and ultra-violet ranges. This noise scales with the electrical volume of the device. Thus, employing light resonators can serve as a strategy to decouple the optical area from the electrical volume. B. Zhu et al. proposed a strategy where fiber couplers act as photon funnels into a photoconductive device made of HgTe CQDs (**Figure 14**a).[180] An important aspect of this endeavor involving resonators is their transfer to the FPA level. However, this transition brings new constraints, particularly related to the limited in-plane space, restricting the use of quasi-infinite gratings. As a result, only vertical Fabry-Perot cavities have been implemented on the FPA[42,45] (as shown in Figure 14b,c). Future works in this area would need to focus on designing specific resonators compatible with limited pixel sizes (2–15 µm for SWIR). Another challenge faced by MWIR CQDs arises when used for wavelengths where conventional transparent conductive oxide (TCO) starts to exhibit limited transmission (typically above 2 µm). To address this, a trade-off involves thinning the indium tin oxide (ITO) layer to reduce its absorption, but this leads to higher contact resistance. An alternative approach proposed by T. Dang et al. replaced the TCO layer with a resonant grating[50] (illustrated in Figure 14d). Leveraging resonance enables achieving transparency beyond the filling factor of the layer, resulting in improved responsivity in the MWIR, as seen in Figure 14e.

4.1.3. Emergence of Active Devices

The introduction of light resonators presents a new degree of freedom in shaping the spectral response of CQDs, expanding beyond the size tunability resulting from quantum confinement. However, the capability to alter the spectral response post-fabrication was a missing element until recently. The field of active photonics had primarily been confined to systems likemicroelectromechanical systems MEMS, where geometrical factors can be actively tuned, or involved phase-change materials. However, T. Dang et al.[174,176,186] noticed that CQD arrays coupled to photonic cavities could offer a new platform for active tunable photonics.

To achieve this, two key ingredients are required: a bias-dependent diffusion length, a property inherently present in CQD arrays;[187] and an absorption map that exhibits spectral inhomogeneity, a role fulfilled by the photonic cavity. By leveraging this concept, researchers have achieved spectral shifts, changes in magnitude,[186] and complete extinction of specific spectral ranges, as shown in Figure 14f.[178]

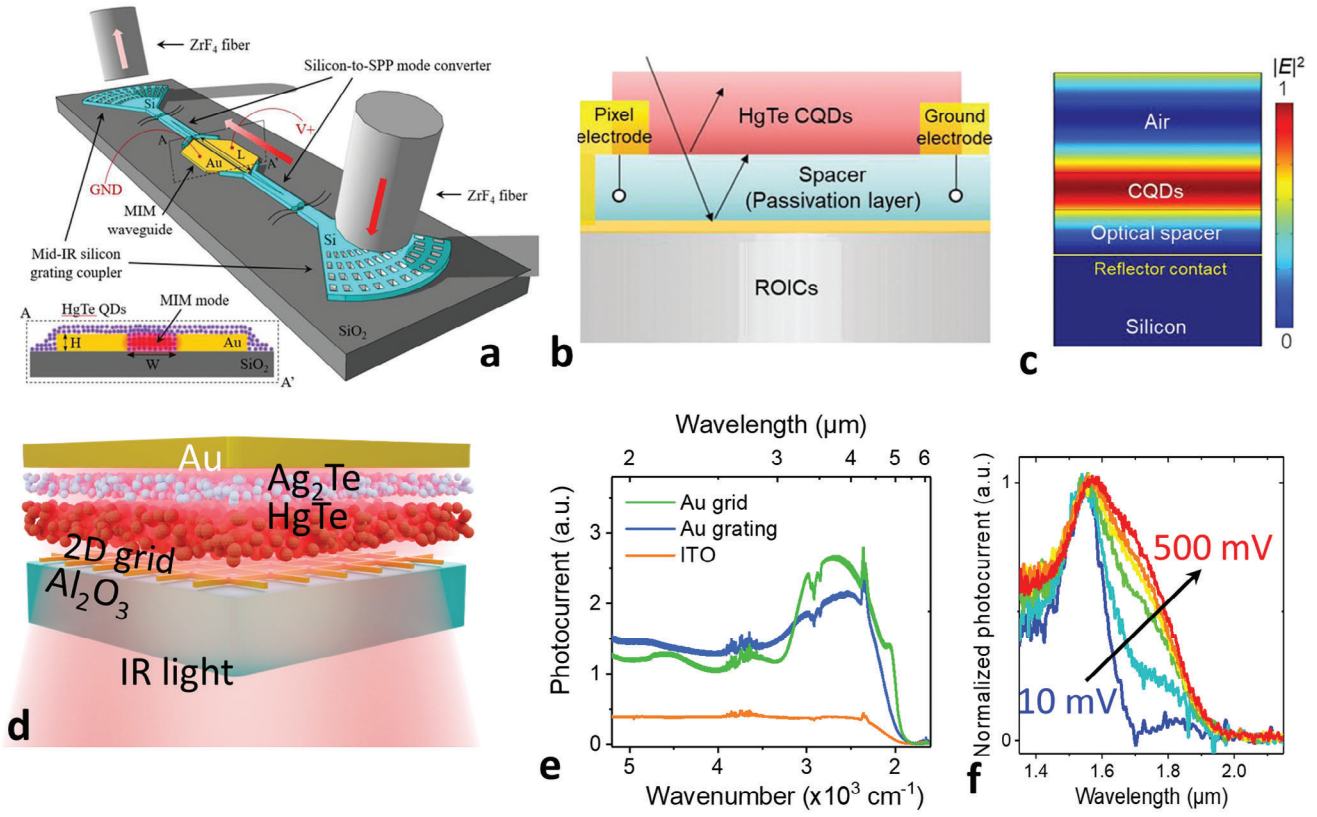

Figure 14. Light resonators in the context of advanced IR detection. a) Schematic of a HgTe CQD photodector coupled to a waveguide acting as a photon funnel. Part a) is adapted with permission from ref. [180]. b) Schematic of a read-out circuit coupled to a HgTe CQD film through a dielectric spacer used to generate a Fabry-Perot cavity. c) Absorption map for the device described in part (b). Parts b) and c) are adapted with permission from ref. [42]. d) Schematic of a diode which MWIR active layer is made of HgTe CGDs and the partly transparent electrodes are made of a resonant metallic grating. e) Photocurrent spectra for the diode depicted in part d), where the bottom electrode is ITO, a 1D or a 2D resonant metallic grating. Parts d) and e) are adapted with permission from ref. [50]. f) Photocurrent spectra under different biases from a HgTe CQD film coupled to a grating with two patterns per grating. Part f) is adapted with permission from ref. [178].

5. From Single Detector to Focal Plane Array Imagers

This chapter is dedicated to the most advanced integration of HgTe CQDs, that is their use for IR imagers,[188,189] starting with a brief overview of progresses done at the single pixel. To date HgTe and PbS CQDs remain the only two colloidal materials for which integration has been pushed up to the imager level. In this regard, PbS is certainly more advanced since it has benefited from the massive effort made on this material to push solar cell performances. This effort has in particular led to the development of efficient diode stacks. Furthermore, PbS possesses dielectric constant, which brings benefits of a weak exciton binding energy that makes electron-hole pairs behave as quasi free charges. Drawbacks of PbS relate to its tendency for slow response times and prompt oxidation. Nevertheless, in the near and short-wave infrared, PbS is certainly a key competitor to HgTe CQD-based devices. This is however no longer the case in the MWIR since in this range lead chalcogenides become limited by their bulk band gap.

Various device structures have been investigated for HgTe CQD photodetectors. In 2011, the spectral sensing range of HgTe CQDs was, for the first time, extended to MWIR (3–5 μm).[35] By depositing HgTe CQDs onto a pair of interdigitated electrodes, photoconductive MWIR HgTe CQD detectors were fabricated. At 130 K, a specific detectivity of 2×10^9ones was demonstrated with a cut-off wavelength at 5 μm.[35] In 2014, the spectral sensing ranges of photoconductive HgTe CQD detectors were further extended into the LWIR (8–12 μm) with a specific detectivity of 1.3×10^9 Jones at 6.5 μm and 6.5×10^6 Jones at 12 μm at cryogenic temperature.[27] To further improve the device performance of photoconductors, optical resonant nanostructures and carrier mobility improvements are both feasible strategies. By integrating HgTe CQDs with optical nano-antenna structures, the specific detectivity of HgTe CQD photoconductors at 80 K was successfully enhanced to 1.5×10^{10} Jones at 5 μm in 2017.[170] With ligands engineering, the carrier mobility of HgTe CQDs was significantly improved by 100-fold, and a specific detectivity of 5.4×10^{10} Jones at 4.8 μm was reported in 2019.[70] Besides that, introducing internal gain mechanism into photoconductors is also an efficient way to boost the photoresponse. HgTe CQD phototransistors with 2D materials[190] and trapping-mode photoconductors[43] have all been proposed. Their working principle is similar: the trapping of minority carrier leads to elongated lifetime of majority carriers, which results in considerable photoconductive gains. However, due to narrow energy band gaps

of IR CQDs or highly conductive nature of 2D materials, the suppression of dark currents in IR photoconductors and phototransistors is challenging and the presence of dark currents lead to substantial noise, which inevitably lower the signal-to-noise ratio. Therefore, despite significant improvements having been achieved, the typical specific detectivity of photoconductive HgTe CQDs reaches the high 10^{10} Jones range at room temperature in the SWIR,[163] which is still behind by one or two order(s) of magnitude compared to the performance of state-of-the-art bulk semiconductors like HgCdTe,[191,192] InGaAs,[193,194] InSb,[195,196] and alternatives such as quantum wells[197–199] and type-II superlattices.[200,201]

To further optimize the device performances, photodiodes have been proposed by coupling HgTe CQDs with a silver layer that likely transforms into Ag_2Te as *p*-type layer in 2015.[202,203] This led to background-limited infrared photodetection (BLIP) performance with a specific detectivity of 4.2×10^{10} Jones at 5.2 µm at an operating temperature of 90 K

The procedure was later optimized by directly coupling Ag_2Te nanocrystals to the HgTe CQD layer. With the successful construction of a built-in electric field, the HgTe CQD photodiodes can operate under zero bias voltage, which eliminates the dark currents. A $HgCl_2$ solution post-processing method was introduced to react with the deposited Ag_2Te nanocrystals, which released Ag^+ ions and fixed them on the surface of the HgTe CQDs as AgCl.[29,204] After $HgCl_2$ solution treatment, the peak responsivity of the MWIR HgTe CQD photodiode reached 0.56 A W^{-1} at 160 K. In 2023, by reducing the series resistance of HgTe CQD photodiodes, the room-temperature quantum efficiency of MWIR HgTe CQDs was improved to 10% and 15% for HgTe CQDs with cut-off wavelength at 4.2 and 3.7 µm, respectively.[183] Background-limited photodetection performance at 150 K and a detectivity above 10^9 Jones at room temperature was achieved with a cut-off wavelength at 3.7 µm. More importantly, the combination of Ag_2Te nanocrystals and $HgCl_2$ solution treatments not only worked for MWIR HgTe CQDs, but also facilitated the development of SWIR HgTe CQD photodiodes. High-performance photodiodes with cut-off wavelength into the extended SWIR ranges were demonstrated with specific detectivity up to 10^{11} Jones at room temperature.[161,205,206]

The rapid advance of HgTe CQD single-element photodetectors motivated the realization of HgTe CQD FPA imagers. Besides high performance, the solution processability of HgTe CQDs enables monolithic integration with silicon integrated readout circuits (ROICs), resulting in simple and wafer-scale CMOS-compatible fabrication to obtain large array format imagers with small pixel pitch.

Early studies on HgTe CQD FPAs started from photoconductive imagers. By sequential spin-coating of HgTe CQDs onto silicon readout circuits with pre-defined electrodes, a 320 × 256 resolution imager with 30 µm pixel pitch was fabricated[207] and demonstrated a specific detectivity of 1.4×10^9 Jones and noise equivalent temperature difference (NETD) of 2.3 K at an operating temperature of 95 K in 2016. By improving CQD film preparation technique, the NETD of photoconductive HgTe CQD FPAs was further improved to 102 mK at 100 K.[32] 95% of the pixels exhibit a NETD below 280 mK, and the operable pixel rate was ≈99%. In 2023, the resolution of MWIR HgTe CQDs-based FPA imagers was improved to 640 × 512 pixel arrays[208] with pitch of 15 µm, as shown in **Figure 15a**. The cut-off wavelength of the MWIR HgTe CQD imager shifted from 3.8 and 4.6 µm from 300 to 80 K, covering the MWIR atmospheric window (Figure 15b). By employing trapping-mode photoconductive configuration and reducing film thickness non-uniformity, the 640 × 512 MWIR FPA imagers exhibited impressively low photoresponse non-uniformity (*PRNU*) down to 3.42%, high detectivity of 1.5×10^{10} Jones, and high operable pixel rate of 99.99% with only 22 non-effective pixels at 80 K (Figure 15c–e). Later, based on the same device configuration, megapixel 1280 × 1024 array format MWIR HgTe CQD imager[209] was also developed and high-resolution thermal images of humans were captured with NETD down to 30 mK (Figure 15f).

Besides MWIR imagers, SWIR FPAs have also been extensively investigated for their great potential in wafer inspection, composition identification, and autonomous driving. In 2019, VGA-format SWIR HgTe CQD FPA imagers with cutoff wavelength of 1.7 µm were fabricated and demonstrated laser beam profile imaging (**Figure 16a**).[88] Later, in 2022, 640 × 512 pixel format photoconductive imagers were reported (Figure 16b).The spectral sensing range was further extended to 1.8 µm with an EQE of 4%–5% (15% internal quantum efficiency) under Peltier cooling (Figure 16c).[44] The FPA is compatible with 200 fps imaging in full frame, and imaging up to 340 fps was demonstrated by driving a reduced area of the FPA. Various SWIR images were captured by the HgTe CQD-based FPA imagers. The visible and SWIR images of a Si wafer (i and ii), chemical solvents (i-ii, iv-vi), and a soldering iron (iii) are as shown in Figure 16d.

In 2023, R. Alchaar et al. developed a photovoltaic SWIR HgTe CQDs imager.[45] The surface of silicon ROICs was planarized by metal deposition and chemical mechanical polishing, enabling the fabrication of a SWIR HgTe CQD photodiode.[44] This photodiode consisted of SnO_2 (electron transport layer)/HgTe/Ag_2Te (hole transport layer) structure and could be operated in either an inverted (Figure 16e) or a non-inverted configuration. Besides, the HgTe CQDs diode with optimized thickness sandwiched between the pixel electrode and the semitransparent top gold electrode formed a Fabry-Perot cavity, enabling effective absorption enhancement of up to 50% at the CQD band edge (Figure 16f). Compared with the photoconductive HgTe CQDs, the photovoltaic HgTe CQDs imager presented lower dark currents. As a result, the SWIR imaging quality was significantly improved compared with photoconductive ones. Images of chemical solvents, human face, and ISO12233:2000 chart were captured by the photovoltaic HgTe CQDs-based FPA at −40 °C (Figure 16f).

SWIR HgTe CQDs with lateral *p-n* junctions were reported in 2023.[46] Applying a bias across HgTe CQDs deposited onto a pair of electrodes results in controllable lateral p-n junctions (see method relative to ref. [46]) which could be induced to turn a photoconductor to a lateral photovoltaic detector (**Figure 17a**) through the formation of a planar *p-n* junction thanks to the gates.[63,210,211] The doping level and nature can be adjusted by changing the polarity and the activation time of the applied electric field. The SWIR HgTe CQD–based detectors with planar *p-n* junctions were successfully monolithically integrated with a CMOS ROIC with a 640 × 512 pixels array (15 µm pixel pitch) and exhibited a detectivity of 3×10^{10} Jones (Figure 17b). Benefitting from the presence of built-in potential and depletion re-

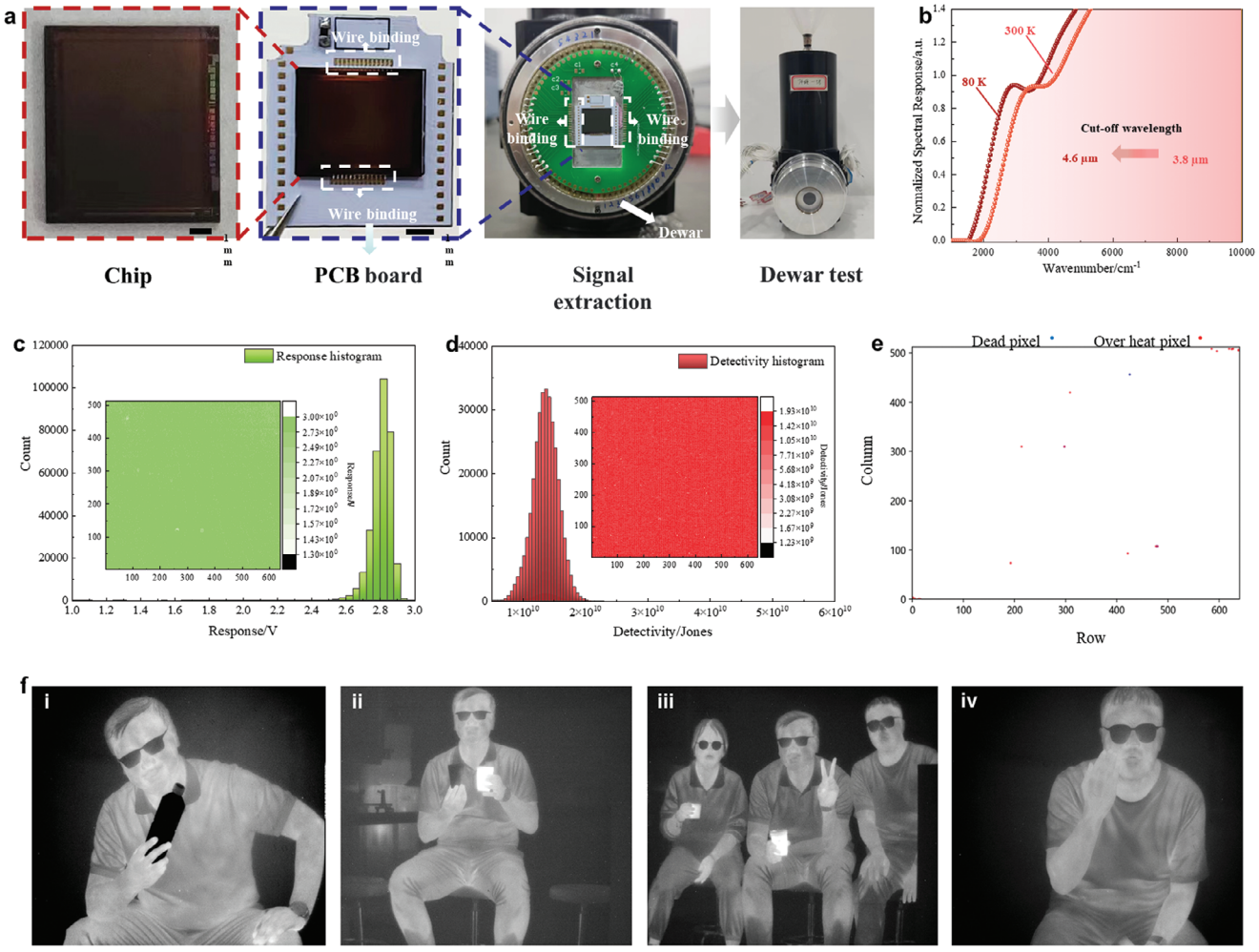

Figure 15. Trapping-mode photoconductive MWIR HgTe CQDs-based FPA imagers. a) Diagram of device signal extraction and Dewar test package of a 640 × 512 MWIR imager.[208] b) Response spectra of MWIR HgTe photodetectors at room temperature and 80 K.[208] c) Response distribution diagram and response statistics histogram of the 640 × 512 format imagers.[208] d) Detectivity distribution diagram and detectivity statistics histogram the 640 × 512 format imagers.[208] e) Overheated pixels and dead pixels mapping of a FPA with the 640 × 512 format.[208] f) Megapixel thermal images captured by the 1280 × 1024 MWIR FPA imagers.[209] The f-number is 2, and NETD is 30 mK.

gion, the dead pixel rate and overheat pixel rate were both reduced (Figure 17b–d). High-resolution SWIR infrared imaging was also demonstrated, showing great potential for various applications including semiconductor inspection, food safety, and chemical analysis (Figure 17e).

SWIR HgTe CQD FPAs in trapping-mode photoconductor configuration have also been investigated. The concept of a trapping-mode photoconductor consisting of an intrinsic CQDs layer as the main sensing channel and a doped layer on top of the intrinsic one (**Figure** 18a) was applied.[43] The minority carriers were trapped by a vertical built-in potential leading to both decreased dark current density and improved quantum efficiency. Without using the top metallic electrode, the optical loss introduced by the reflection from the top contact is avoided. The trapping-mode SWIR HgTe CQD CMOS imagers showed *PRNU* down to 4%, dead pixel rate of 0%, *EQE* up to 175%, and detectivity as high as 2×10^{11} Jones for SWIR (cut-off wavelength = 2.5 μm) at 300 K. High-quality SWIR images were also demonstrated at room temperature, as shown in Figure 18b. In order to improve the spatial resolution of SWIR HgTe CQD-based FPA imagers, a megapixel (1280 x1024 pixel) SWIR FPA imager was fabricated with an in-pixel resonant cavity.[212] Utilizing the passivation layer of the CMOS chip and the underlying metal contacts on the ROICs, an in-pixel resonant cavity was constructed to enhance the absorption and spectral selectivity of the HgTe CQD film (Figure 18c). With the megapixel format imager, high-resolution SWIR imaging was demonstrated, and the resolution of the imager could be as good as 40-line pairs per millimeter (lp/mm) (Figure 18d). Through optimizing the homogeneity of the CQD films, the operable pixel factor of the SWIR HgTe CQD-based FPA imagers reached 99.99%.

Beside single-color detection, multi-band HgTe CQD detectors have been investigated by combining materials with various energy gaps. SWIR/MWIR,[162,214,215] visible/SWIR,[216–218] and SWIR/SWIR/MWIR[219] HgTe CQDs detectors have been reported. In 2022, a CQD-based CMOS-compatible multispectral

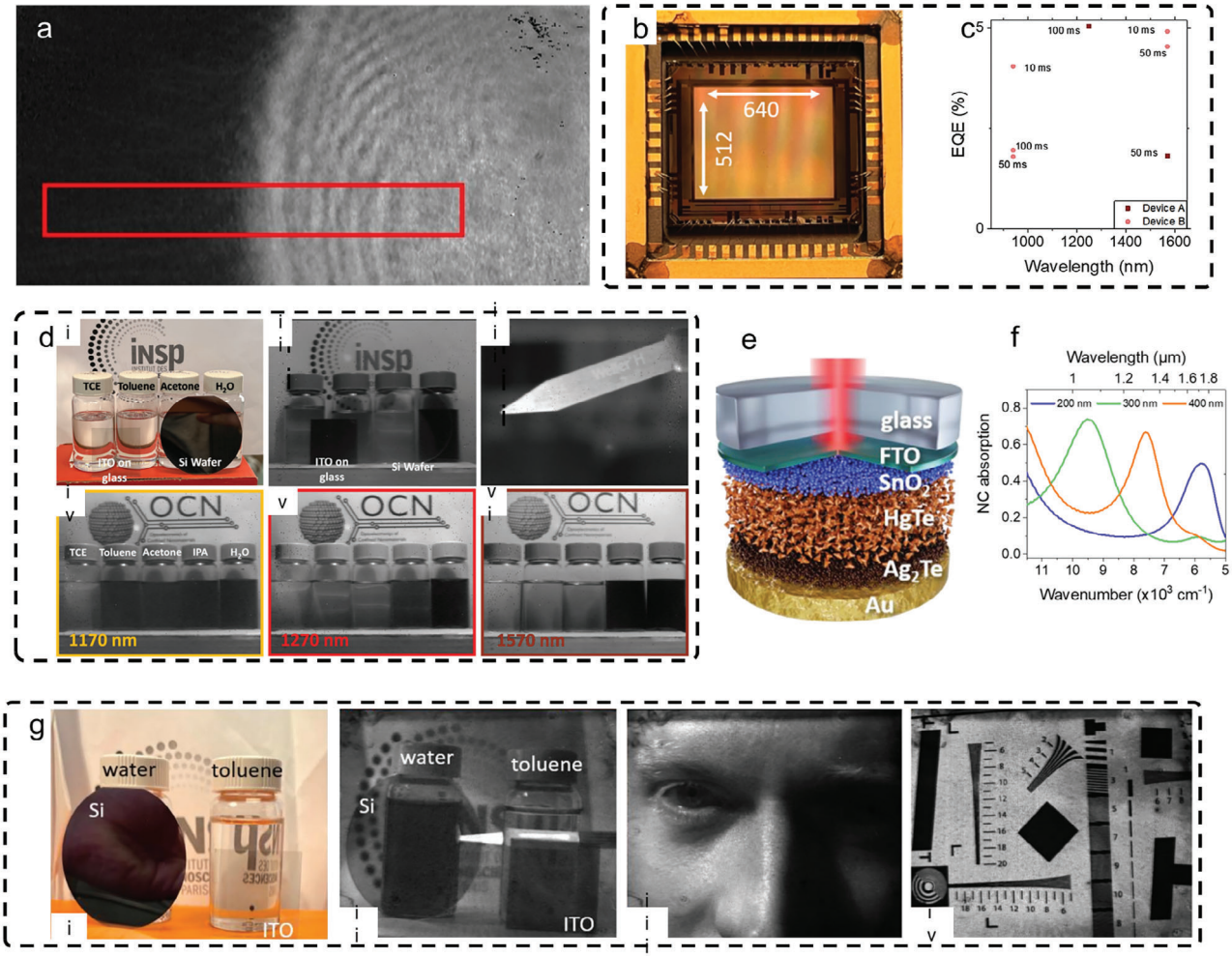

Figure 16. Photoconductive and photovoltaic SWIR HgTe CQD-based FPA imagers. a) Image of the laser beam taken with VGA read out circuit surface.[88] b) Picture of the ROIC in the ceramic lead-less chip carrier after deposition of the CQD film.[44] c) EQE of the HgTe CQD camera as a function of the wavelength and the exposure time for two different devices.[44] d) SWIR imaging using HgTe CQD-based FPA.[44] e) Schematic of the diode stack used for SWIR sensing. f) Simulated absorption spectra of SWIR HgTe CQDs for three thicknesses of the HgTe layers. g) i) Visible image of a scene containing a Si substrate and an ITO substrate in front of two vials filled with transparent liquids in the visible; ii) SWIR image from the same scene as in i); iii) image from a face and iv) from a ISO-12233 test chart by a photovoltaic HgTe CQDs-based FPA imagers.[45]

imager was reported with spectral response from the ultraviolet (UV) and visible to SWIR.[213] The direct optical lithography of down-conversion perovskite QDs and SWIR HgTe CQDs onto a Si imager was conducted to construct two channels of UV-enhanced visible pixels and SWIR pixels (Figure 18e). High-resolution single-color images and merged multispectral images were obtained by using only one CQD-based FPA imager (Figure 18f). The multispectral CQD-based FPA imager exhibited excellent performance with *PRNU* of below 5%, dead pixel rate of 0%, and room-temperature responsivities of 0.25 A W^{-1} at 300 nm, 0.4 A W^{-1} at 750 nm, and 0.25 A W^{-1} at 2.0 μm.

Currently, array-format imaging is mainly achieved by integrating CQDs with ROICs, and the recent progress of SWIR and MWIR HgTe CQD-based FPA imagers is summarized in **Table 1**. Despite the key role played by ROICs play in HgTe CQD imagers, their use could limit the resolution, pixel pitch, and mechanical flexibility of HgTe CQD imagers. To realize infrared imaging, infrared-to-visible upconverters provide a potential route toward large-format, high-resolution, pixel-less infrared images without bringing in readout integrated circuits, thus arousing broad attention. By using SWIR HgTe CQDs as the sensing layer and optimizing matching the photodetector units and visible light-emitting units, the infrared-to-visible upconversion devices demonstrated a SWIR detection of 2.5 μm cut-off wavelength, a high upconversion efficiency of nearly 30% and specific detectivity of nearly 5.6×10^5 Jones (with bandwidth of 125 Hz).[220]

6. Outline for the Transfer from the Lab to Industry

While the development of HgTe CQDs has seen a lot of progress over the last decade, significant challenges remain to see them transitioning into marketable products. Future efforts to advance the maturity of HgTe CQDs-based sensors and arrays will benefit from i) better clarity in the proposition for low-cost manufacturing and identification of customers and markets; ii) increased

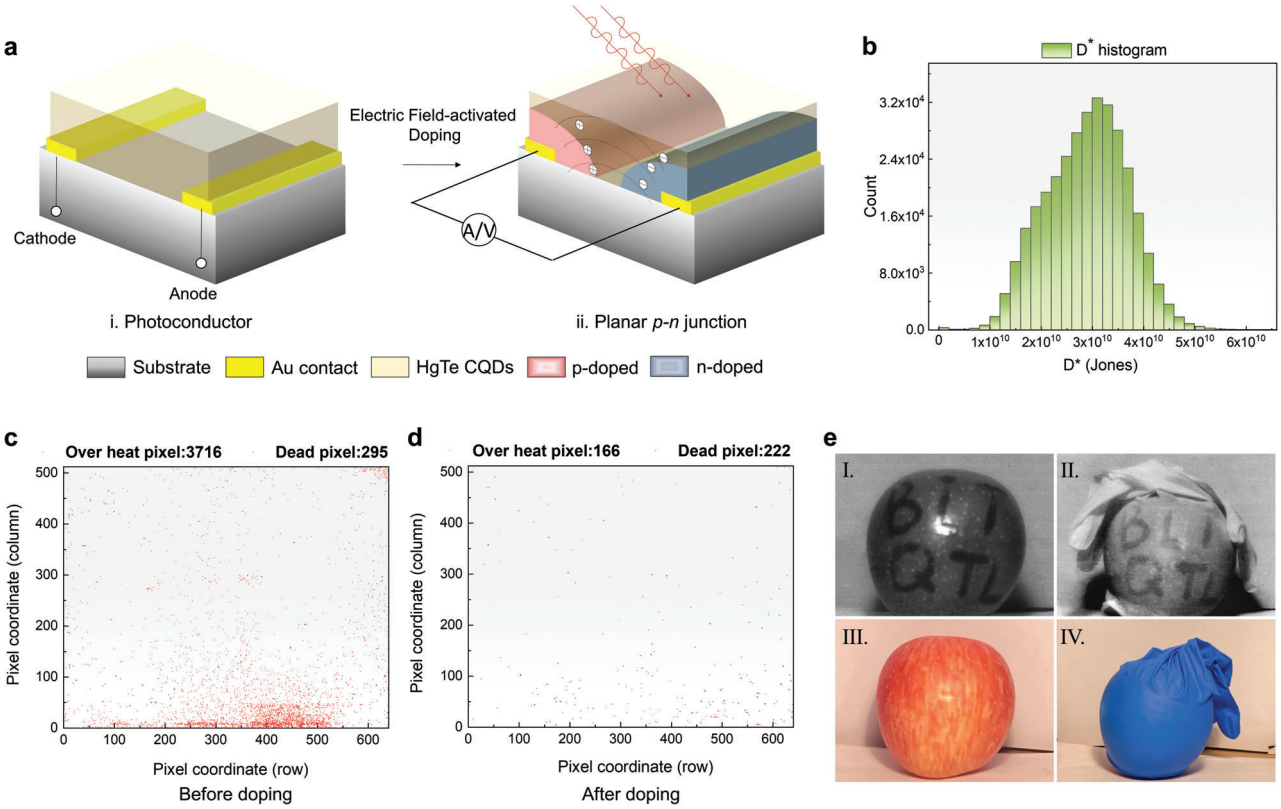

Figure 17. SWIR HgTe CQD FPA imagers with lateral p-n junctions. a) Schematic diagram of the detector operation from PC mode to PV mode with planar p-n junctions after in situ electric field–activated doping.[46] b) Histogram of detectivity of the planar p-n junction FPA imagers.[46] Overheated pixels and dead pixels of the FPA imagers c) before doping and d) after doping with planar p-n junctions.[46] e) SWIR and visible images of the apple with the "BITQTL" words on the surface (I and II) and the apple inside the nitrile glove (III and IV).[46]

modeling or empirical correlations between application and detector level performance metrics; and iii) process development for improved reproducibility and stability.

The common proposition made for CQD materials in IR detection and imaging is lower manufacturing costs compared to conventional materials such as InGaAs and HgCdTe. Solution synthesis and processing can certainly be done at significantly lower cost than vacuum methods of physical or chemical vapor deposition. However, the impact of this will be better understood in the context of the full system cost. As a sake of example, for MWIR ROICs, cooling, and optics have a higher share of the total cost than in SWIR which lessens the impact of a lower cost FPA.

Few examples of cost models were reported in the literature for either HgTe CQDs or conventional IR technologies. C. Greboval et al. recently estimated the cost of CQD FPA fabrication at only 10–20 €, which was compared to InGaAs arrays at 600 € with an additional 600 € for the camera lens.[44] Building costs for HgCdTe cameras are not broadly available but a model reported in 2003 gave ≈3 k USD for a 256 × 256 FPA with the detector array and the hybridization contributing the majority of the cost.[221]

Furthermore, the upfront cost to set up a manufacturing environment and develop processes is on the order of at least several million USD, and the return on investment (ROI) timeline is uncertain without better projections. Any benefit of lower manufacturing costs is shared between the profit margin and the product price. If performance can be improved to match conventional technologies, target market shares or new market volumes can be more readily estimated, lowering risks for financial investments needed to advance to higher technology readiness level. More likely in the short term, lower performance sensors at a lower cost may take market shares or grow new markets where the best available performance is not needed. To engage with those market segments, however, models of system and application performance based on manufacturable detector performances, or better yet, minimum viable product (MVP) demonstrations are needed. If bottomline performance cannot meet application requirements, no manufacturing cost will be low enough.

To get to MVP, however, process development is needed to improve reproducibility and stability. Often, extended effort is needed to reproduce literature results in the industrial setting, and this is especially true with scaling up in volume and to wafer processing. It is often tempting to reproduce record reported performance before completing engineering necessary to make the process robust. A balance must be struck though to avoid a common pitfall of iterating on a poorly controlled process. One of many challenges faced in making the transition to product development is funding this process improvement which often falls in a gap between basic research with frequent articulable progress and tolerable ROI with sales in sight. For smaller businesses, government contracts offer some support but require alignment or effective lobbying with program managers. A clear picture of

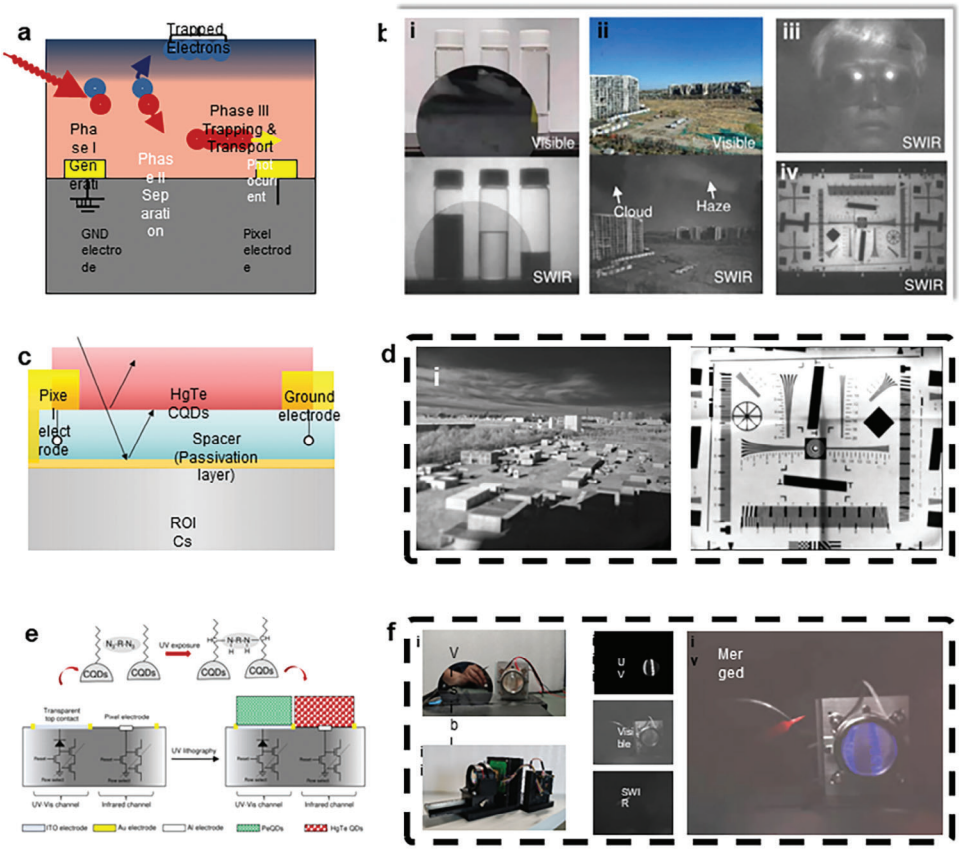

Figure 18. Trapping-mode photoconductive SWIR HgTe CQD-based FPA imagers. a) Illustration of the working process of trapping-mode photodetectors.[43] b) SWIR images captured with a HgTe CQD-based FPA imagers at room temperature.[43] i) visible and SWIR images of three bottles of water, tetrachloroethylene, and isopropanol behind a Si wafer. ii) Visible and SWIR images of sky and buildings. iii) SWIR image of a human face with glasses. iv) SWIR image of an ISO-12233 test chart. c) The cross-section showing the in-pixel resonant cavity.[212] d) Photograph of outdoor buildings i and ii) and ISO-12233 test chart iii) captured by the imagers at room temperature.[212] e) Schematic illustration of the ligand cross-linking process and the configuration of a UV-enhanced visible pixel and SWIR pixel.[213] f) Multispectral CQD imagers.[213] i) Multispectral CQD imagers and peripheral circuits. ii) Imaging scene: a soldering iron, a Si wafer, and a UV lamp. iii) Captured UV–vis, and SWIR images. iv) Merged multispectral images with a UV image as the blue channel, visible light as the grayscale channel, and a SWIR image as the red channel.

future customers and market knowledge is typically needed to justify internal or external investment.

Several companies have made or have ongoing development efforts in HgTe CQDs-based SWIR and MWIR sensors and arrays. Some of these are listed in **Figure 19** and in **Table 2**, where two suppliers of SWIR CQDs and several companies working with PbS CQDs for SWIR applications are also included. Currently available sensor products on the market include PbS CQDs-based SWIR cameras from SWIR Vision Systems, ST Microelectronics, and Emberion, along with a SWIR FPA from Quantum Solutions. For HgTe, the first MWIR video was reported in 2016 from Sivananthan Laboratories; a significant milestone, while still in early development.

The markets for CQDs-based infrared sensors are uncertain or underdeveloped and both identifying customer needs and aligning the technological capabilities to these needs are required to see the markets grow. CQDs for visible colors in displays, a much more mainstream market, even if expanded color gamut was not immediately recognized as necessary, were worked on for a decade in industry before they saw large growth in 2015.

The development of PbS CQDs for SWIR has a longer history and offers some guidance for those working with HgTe CQDs. Wafer-scale fabrication with PbS CQDs was a significant milestone that was reported only in the last 5 years by IMEC,[222] ST Microelectronics,[223] and others. Fabrication of HgTe CQDs-based photodetector arrays with a lateral geometry that is more robust to film defects and non-uniformity has been reported on 8 inch wafers.[43,46] The proper way to actually perform the coupling between the ROIC and the CQD layer remains unclear to date. Wafer level processing has the clear benefit of enabling mass production, which is critical to address mass market development, such as sensors for smartphones, a market where the cost per device needs to be brought down to a few dollars per chip. However, the current model actually chosen by many companies producing CQDs-based infrared cameras is rather to go toward high performing cameras and bring a complementary value with respect to InGaAs, with none or very modest cost disruption compared to the historical technologies. Such a commercial model matches the current ones from the SWIR field with only a few thousand cameras sold per year. It then becomes actually

Table 1. The performance comparison of SWIR and MWIR HgTe CQDs-based FPA imagers.

Spectral ranges	Year and reference	Operating mode	Cut-off wavelength (μm)	Resolution	Pixel pitch (μm)	Operation temperature	Detectivity (Jones)	*EQE* (%)	*PRNU* (%)	*NETD* (mK)
SWIR	2019[88]	–	1.7	549 × 254	–	–	–	–	–	–
	2022[44]	PC	1.8	640 × 512	15	−32 °C	–	4–5	–	–
	2022[213]	Trapping-mode	2.5	320 × 256	30	Room-temperature	–	–	5	–
	2023[45]	PV	1.9	640 × 512	15	−40 °C	–	0.33	–	–
	2023[43]	Trapping-mode	2.5	320 × 256	30	Room-temperature	2×10^{11}	175	4	–
	2023[212]	PC	2	1280 × 1024	15	Room-temperature	2.8×10^{10}	14	–	–
	2023[46]	Lateral p-n junctions	2.5	640 × 512	15	Room-temperature	3×10^{10}	25 ± 2	–	–
	2016[207]	PC	5	320 × 256	30	95 K	1.46×10^{9}	0.3	–	2319
MWIR	2016[32]	PC	5	320 × 256	30	100 K	–	0.64	–	102
	2023[43]	Trapping-mode	5.5	320 × 256	30	80 K	8×10^{10}	–	–	–
	2023[208]	Trapping-mode	4.6	640 × 512	15	80 K	2×10^{10}	–	3.42	51.26
	Year and reference	Operating mode	Cut-off wavelength (μm)	Resolution	Pixel pitch (μm)	Operation temperature	Detectivity (Jones)	*EQE* (%)	*PRNU* (%)	*NETD* (mK)

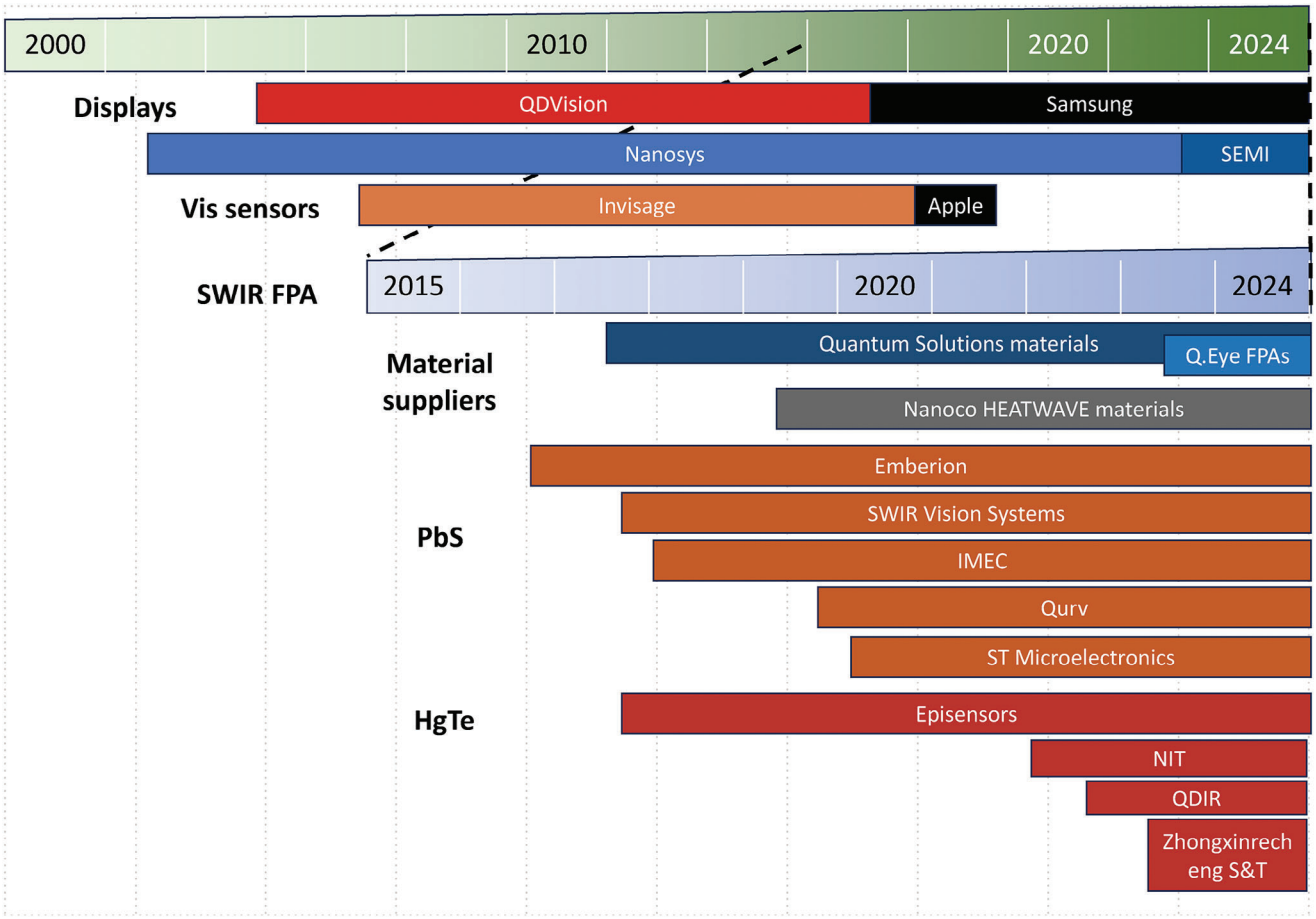

Figure 19. Timeline of the different companies involved in the development of CQD based products, including those based on HgTe CQDs.

Table 2. Companies involved in the development and commercialization of CQDs-based infrared imagers.

Company	Location	Product	Material	Spectrum	Status
Nanoco	UK	Material	PbS, InAs	SWIR	Commercial
Quantum Solutions	UK	Material	PbS, InAs,	SWIR	Commercial
QustomDot	Belgium	Material	PbS, InAs,	SWIR	Commercial
Quantum science	UK	Material	PbS, Ag_2S, Ag_2Se	SWIR	Commercial
Mesolight	China	Material	PbS	SWIR	Commercial
Nanografi	Turkey	Material	PbS	SWIR	Commercial
Quantum Solutions	UK	FPA	PbS	SWIR	Commercial
SWIR Vision Systems	US	Camera	PbS	SWIR	Commercial
Emberion	Finland	Camera	PbS	SWIR	Commercial
STMicro	Fr, IT, US	Camera	PbS	SWIR	Development
IMEC	Belgium	FPA	PbS	SWIR	
Qurv	Spain	camera	PbS-Ag_2Te	SWIR	Development
QDI systems	Netherlands	FPA	PbS	SWIR	Development
QDIR	US	FPA	HgTe	MWIR	Development
Zhongxinrecheng Science and Technology Co. Ltd.	China	FPA and Camera	HgTe	SWIR, MWIR	Commercial
Sivananthan Labs	US	Camera	HgTe	SWIR, MWIR	Development
New Imaging Technologies	France	Camera	HgTe	SWIR	Development

very questionable if wafer level processing is actually the relevant strategy, since die level manufacturing is still compatible with the work of a single operator. Additionally, die level processing probably offers more tunability in term of processing. Nevertheless, the high value strategy will be a losing strategy as soon as one of the industrial companies chooses to drop the market price.

One would have noticed that both PbS and HgTe share the similarity of containing heavy metal which has been seen as a deal breaker in the visible when it comes to the transfer to industry. Though being a non-desirable situation, it is worth pointing out that infrared CQD-based cameras already bring a significant reduction in the quantity of heavy metal/toxic atoms used compared to their epitaxially grown counterpart. Indeed, by lifting the constrain of epitaxy, deposition of CQD can be handled directly on the CMOS circuit without the need of an intermediate substrate made of CdZnTe or GaAs. Furthermore, the materials are processed at comparatively reduced temperatures (below 120 °C for HgTe and below 150 °C for PbS) which also reduces the energy cost associated to the material growth. If ever a more drastic reduction of toxic content was targeted, the solution should certainly be inspired from the effort conducted for displays, for which the efforts have been focused on a transition from II-VI semiconductors to III-V materials (InP in the case of displays). However, the equivalent effort based on InAs and InSb is still at the early stage,[224–231] meaning that the focus remains mostly on growth methods, expanding the range of sizes to push toward redder wavelengths and solving stability issues. This certainly contrasts with the higher maturity of PbS and HgTe for which more advanced achievements are now routinely reported. There is certainly room for both at this stage, with PbS and HgTe acting as a mature platform for prototyping while material developments target stable III-V (or other) infrared CQDs.

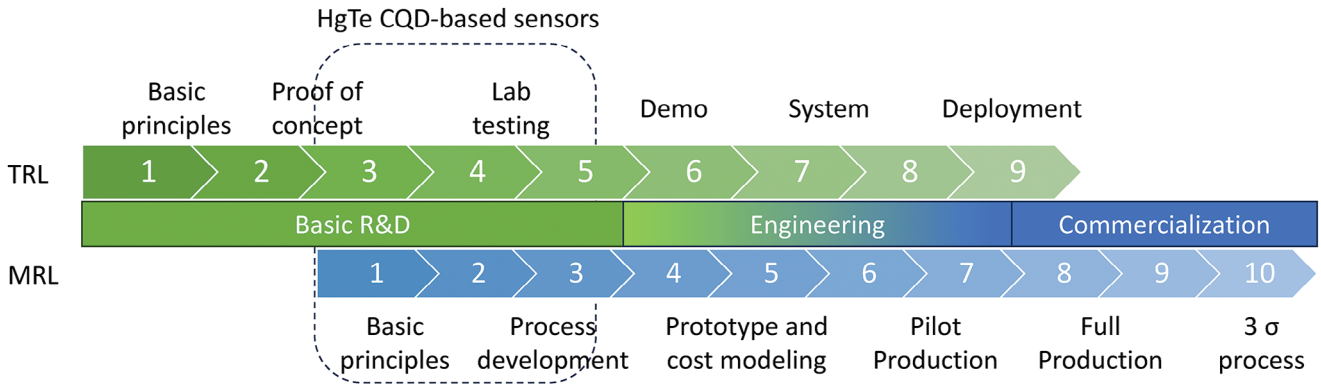

Figure 20. Technology readiness level for HgTe CQD based focal plane arrays.

Technology or manufacturing readiness level (TRL or MRL, see **Figure 20**) is often used to describe status on the development path. The exact definition of stages on these scales varies but both start at a value of 1 with basic principles identified and finish at 9 or 10 in production. Reported HgTe CQD based sensors are currently somewhere in the range of TRL 3–5 and MRL 1–3 (lower for MWIR). Moving these values forward will require a clearer target market, continued performance and stability improvements, and process development.

7. Conclusions

HgTe CQDs and their IR device applications are experiencing a rapid growth. This is despite the known toxicity of Hg, and the concerns this toxicity raises for eventual widespread commercial applications. The present interest is motivated by the ease of entry compared to traditional epitaxial technologies, the rapid advances in detector performance and the stunning demonstrations of IR imagers. HgTe CQDs allow for first explorations in the field of solution-based IR nanomaterials, promising a transformation of the IR technologies while also raising new questions of basic academic interest. Furthermore, to date, it remains the only platform able to cover the mid-infrared based on interband transitions, as opposed to current alternatives (mostly HgSe[232] and Ag_2Se)[233–236] that rely on intraband transitions and for which the reported performances lag two orders of magnitude behind.

As more groups study this versatile IR platform, new synthetic paths for HgTe CQDs are developed enabling increased control over their shape, phase and size. Core/shell and heterostructures based on the HgTe platform can increase in complexity and quality to further optmize the IR response and reduce non-radiative recombination. Much more effort can go into the CQD film fabrication. This includes wafer-scale coatings of films with high optical quality, robust *p-n* junctions, and also much needed innovation in the chemical processing that addresses the atomic details of the interfaces. This is very necessary since these interfaces have so much influence on the key properties of carrier mobility and exciton relaxation. In parallel to chemical advances, integration in photonic or plasmonic structures will enhance light-matter coupling, delivering increased absorption and emission efficiency.

Started as a topic of academic research but motivated by clear high-technology targets, HgTe CQDs reached an impressive level of maturity that enables complex device integration. IR imaging is acting as a flagship for this topic demonstrating the potential of nanocrystal inks as an alternative to traditional epitaxial thin films for IR sensing and emission. The potential of HgTe CQDs is not limited to IR imaging, and other areas such as active photonics and IR light sources will benefit from all the development made around the HgTe CQD platform.

Acknowledgements

This work was supported by ERC grant Ne2Dem (grant number 853049) and AQDtive (grant no.101086358); by French state funds managed by the ANR through the grants Frontal (ANR-19-CE09-0017), Graskop (ANR-19-CE09-0026), Copin (ANR-19-CE24-0022), Bright (ANR-21-CE24-0012-02), MixDferro (ANR-21-CE09-0029), Quicktera (ANR-22-CE09-0018), Operatwist (ANR-22-CE09-0037-01) and E-map (ANR-23-CE50); by National Key R&D Program of China (2021YFA0717600), National Natural Science Foundation of China (NSFC No. 62035004, NSFC No. U22A2081, and NSFC No. 62305022); by the Research Grants Council of Hong Kong SAR (SRFS2324-1S04), and the Innovation and Technology Commission of Hong Kong SAR (ITS/027/22MX).

Conflict of Interest

The authors declare no conflict of interest.

Keywords

camera, HgTe, infrared, light resonator, modelling, nanoparticle growth, optoelectronics

Received: March 27, 2024
Revised: June 7, 2024
Published online: July 18, 2024

[1] C. Gréboval, A. Chu, N. Goubet, C. Livache, S. Ithurria, E. Lhuillier, *Chem. Rev.* **2021**, *121*, 3627.
[2] Y. Tian, H. Luo, M. Chen, C. Li, S. V. Kershaw, R. Zhang, A. L. Rogach, *Nanoscale* **2023**, *15*, 6476.
[3] Q. Hao, H. Ma, X. Xing, X. Tang, Z. Wei, X. Zhao, M. Chen, *Mater* **2023**, *16*, 7321.
[4] A. Rogalski, *Rep. Prog. Phys.* **2005**, *68*, 2267.
[5] M. König, S. Wiedmann, C. Brüne, A. Roth, H. Buhmann, L. W. Molenkamp, X.-L. Qi, S.-C. Zhang, *Science* **2007**, *318*, 766.
[6] B. Chehaibou, C. Abadie, Y. Prado, X. Z. Xu, G. Vincent, B. Gallas, G. Mugny, A. Arnaud, E. Lhuillier, C. Delerue, *J. Phys. Chem. C* **2023**, *127*, 13789.
[7] J. I. Climente, B. Szafran, *ACS Photonics* **2023**, *10*, 3763.
[8] E. Izquierdo, A. Robin, S. Keuleyan, N. Lequeux, E. Lhuillier, S. Ithurria, *J. Am. Chem. Soc.* **2016**, *138*, 10496.
[9] N. Goubet, A. Jagtap, C. Livache, B. Martinez, H. Portalès, X. Z. Xu, R. P. S. M. Lobo, B. Dubertret, E. Lhuillier, *J. Am. Chem. Soc.* **2018**, *140*, 5033.
[10] T. Apretna, N. Nilforoushan, J. Tignon, S. Dhillon, F. Carosella, R. Ferreira, E. Lhuillier, J. Mangeney, *Appl. Phys. Lett.* **2022**, *121*, 251101.
[11] T. Apretna, S. Massabeau, C. Gréboval, N. Goubet, J. Tignon, S. Dhillon, F. Carosella, R. Ferreira, E. Lhuillier, J. Mangeney, *Nanophotonics* **2021**, *10*, 2753.
[12] H. Zhang, R. Alchaar, Y. Prado, A. Khalili, C. Gréboval, M. Cavallo, E. Bossavit, C. Dabard, T. H. Dang, C. Abadie, C. Methivier, D. Darson, V. Parahyba, P. Potet, J. Ramade, M. G. Silly, J. K. Utterback, D. Pierucci, S. Ithurria, E. Lhuillier, *Chem. Mater.* **2022**, *34*, 10964.
[13] X. Lan, M. Chen, M. H. Hudson, V. Kamysbayev, Y. Wang, P. Guyot-Sionnest, D. V. Talapin, *Nat. Mater.* **2020**, *19*, 323.
[14] B. Martinez, J. Ramade, C. Livache, N. Goubet, A. Chu, C. Gréboval, J. Qu, W. L. Watkins, L. Becerra, E. Dandeu, J. L. Fave, C. Méthivier, E. Lacaze, E. Lhuillier, *Adv. Opt. Mater.* **2019**, *7*, 1900348.
[15] M. Chen, X. Xue, T. Qin, C. Wen, Q. Hao, X. Tang, *Adv. Mater. Technol.* **2023**, *8*, 2300315.
[16] M. Müllenborn, R. F. Jarvis, B. G. Yacobi, R. B. Kaner, C. C. Coleman, N. M. Haegel, *Appl. Phys. A* **1993**, *56*, 317.
[17] A. Rogach, S. V. Kershaw, M. Burt, M. T. Harrison, A. Kornowski, A. Eychmüller, H. Weller, *Adv. Mater.* **1999**, *11*, 552.
[18] H. Kim, K. Cho, H. Song, B. Min, J.-S. Lee, G.-T. Kim, S. Kim, S. H. Kim, T. Noh, *Appl. Phys. Lett.* **2003**, *83*, 4619.
[19] É. O'Connor, A. O'Riordan, H. Doyle, S. Moynihan, A. Cuddihy, G. Redmond, *Appl. Phys. Lett.* **2005**, *86*, 201114.

[20] D. S. Koktysh, N. Gaponik, M. Reufer, J. Crewett, U. Scherf, A. Eychmüller, J. M. Lupton, A. L. Rogach, J. Feldmann, *ChemPhysChem* **2004**, *5*, 1435.
[21] H. Kim, K. Cho, B. Park, J.-H. Kim, J. W. Lee, S. Kim, T. Noh, E. Jang, *Solid State Commun.* **2006**, *137*, 315.
[22] H. S. Kim, K. Cho, H. W. Song, J. H. Kim, J. W. Lee, J. S. Lee, B. Min, S. H. Kim, S. S. Kim, *Key Eng. Mater.* **2005**, *277*, 961.
[23] H. Kim, B. Park, K. Cho, J.-H. Kim, J. W. Lee, D.-W. Kim, S. Kim, *Jpn. J. Appl. Phys.* **2005**, *44*, 5703.
[24] H. Kim, K. Cho, D.-W. Kim, B.-M. Moon, M. Y. Sung, S. Kim, *Jpn. J. Appl. Phys.* **2006**, *45*, 7213.
[25] M. V. Kovalenko, E. Kaufmann, D. Pachinger, J. Roither, M. Huber, J. Stangl, G. Hesser, F. Schäffler, W. Heiss, *J. Am. Chem. Soc.* **2006**, *128*, 3516.
[26] S. Keuleyan, E. Lhuillier, P. Guyot-Sionnest, *J. Am. Chem. Soc.* **2011**, *133*, 16422.
[27] S. E. Keuleyan, P. Guyot-Sionnest, C. Delerue, G. Allan, *ACS Nano* **2014**, *8*, 8676.
[28] M. Chen, L. Shao, S. V. Kershaw, H. Yu, J. Wang, A. L. Rogach, N. Zhao, *ACS Nano* **2014**, *8*, 8208.
[29] X. Tang, M. M. Ackerman, P. Guyot-Sionnest, *ACS Nano* **2018**, *12*, 7362.
[30] J. Qu, P. Rastogi, C. Gréboval, D. Lagarde, A. Chu, C. Dabard, A. Khalili, H. Cruguel, C. Robert, X. Z. Xu, S. Ithurria, M. G. Silly, S. Ferré, X. Marie, E. Lhuillier, *Nano Lett.* **2020**, *20*, 6185.
[31] A. S. Portniagin, K. A. Sergeeva, S. V. Kershaw, A. L. Rogach, *Chem. Mater.* **2023**, *35*, 5631.
[32] C. Buurma, R. E. Pimpinella, A. J. Ciani, J. S. Feldman, C. H. Grein, P. Guyot-Sionnest, In **2016**, *Proc. SPIE 9933, Optical Sensing, Imaging, and Photon Counting: Nanostructured Devices and Applications 2016* (Eds.: M. Razeghi, D. S. Temple, G. J. Brown), SPIE, San Diego, California, United States, 993303.
[33] S. Kim, T. Kim, S. H. Im, S. I. Seok, K. W. Kim, S. Kim, S.-W. Kim, *J. Mater. Chem.* **2011**, *21*, 15232.
[34] E. Lhuillier, S. Keuleyan, P. Rekemeyer, P. Guyot-Sionnest, *J. Appl. Phys.* **2011**, *110*, 033110.
[35] S. Keuleyan, E. Lhuillier, V. Brajuskovic, P. Guyot-Sionnest, *Nat. Photonics* **2011**, *5*, 489.
[36] H. Liu, S. Keuleyan, P. Guyot-Sionnest, *J. Phys. Chem. C* **2012**, *116*, 1344.
[37] H. Liu, E. Lhuillier, P. Guyot-Sionnest, *J. Appl. Phys.* **2014**, *115*, 154309.
[38] M. Chen, H. Yu, S. V. Kershaw, H. Xu, S. Gupta, F. Hetsch, A. L. Rogach, N. Zhao, *Adv. Funct. Mater.* **2014**, *24*, 53.
[39] E. Lhuillier, S. Keuleyan, P. Zolotavin, P. Guyot-Sionnest, *Adv. Mater.* **2013**, *25*, 137.
[40] L. Protesescu, S. Yakunin, M. I. Bodnarchuk, F. Krieg, R. Caputo, C. H. Hendon, R. X. Yang, A. Walsh, M. V. Kovalenko, *Nano Lett.* **2015**, *15*, 3692.
[41] J. Qu, M. Weis, E. Izquierdo, S. G. Mizrahi, A. Chu, C. Dabard, C. Gréboval, E. Bossavit, Y. Prado, E. Péronne, S. Ithurria, G. Patriarche, M. G. Silly, G. Vincent, D. Boschetto, E. Lhuillier, *Nat. Photonics* **2022**, *16*, 38.
[42] Y. Luo, Y. Tan, C. Bi, S. Zhang, X. Xue, M. Chen, Q. Hao, Y. Liu, X. Tang, *APL Photonics* **2023**, *8*, 056109.
[43] S. Zhang, C. Bi, T. Qin, Y. Liu, J. Cao, J. Song, Y. Huo, M. Chen, Q. Hao, X. Tang, *ACS Photonics* **2023**, *10*, 673.
[44] C. Gréboval, D. Darson, V. Parahyba, R. Alchaar, C. Abadie, V. Noguier, S. Ferré, E. Izquierdo, A. Khalili, Y. Prado, P. Potet, E. Lhuillier, *Nanoscale* **2022**, *14*, 9359.
[45] R. Alchaar, A. Khalili, N. Ledos, T. H. Dang, M. Lebreton, M. Cavallo, E. Bossavit, H. Zhang, Y. Prado, X. Lafosse, V. Parahyba, P. Potet, D. Darson, E. Lhuillier, *Appl. Phys. Lett.* **2023**, *123*, 051108.
[46] T. Qin, G. Mu, P. Zhao, Y. Tan, Y. Liu, S. Zhang, Y. Luo, Q. Hao, M. Chen, X. Tang, *Sci. Adv.* **2023**, *9*, eadg7827.
[47] A. A. Sergeev, D. V. Pavlov, A. A. Kuchmizhak, M. V. Lapine, W. K. Yiu, Y. Dong, N. Ke, S. Juodkazis, N. Zhao, S. V. Kershaw, A. L. Rogach, *Light: Sci. Appl.* **2020**, *9*, 16.
[48] K. A. Sergeeva, D. V. Pavlov, A. A. Seredin, E. V. Mitsai, A. A. Sergeev, E. B. Modin, A. V. Sokolova, T. C. Lau, K. V. Baryshnikova, M. I. Petrov, S. V. Kershaw, A. A. Kuchmizhak, K. S. Wong, A. L. Rogach, *Adv. Funct. Mater.* **2023**, *33*, 2307660.
[49] S. M. Tenney, V. Vilchez, M. L. Sonnleitner, C. Huang, H. C. Friedman, A. J. Shin, T. L. Atallah, A. P. Deshmukh, S. Ithurria, J. R. Caram, *J. Phys. Chem. Lett.* **2020**, *11*, 3473.
[50] T. H. Dang, M. Cavallo, A. Khalili, C. Dabard, E. Bossavit, H. Zhang, N. Ledos, Y. Prado, X. Lafosse, C. Abadie, D. Gacemi, S. Ithurria, G. Vincent, Y. Todorov, C. Sirtori, A. Vasanelli, E. Lhuillier, *Nano Lett.* **2023**, *23*, 8539.
[51] X. Shen, A. Kamath, P. Guyot-Sionnest, *Nat. Photonics* **2023**, *17*, 1042.
[52] S. V. Kershaw, A. L. Rogach, *Zeitschrift für Physikalische Chemie* **2015**, *229*, 23.
[53] E. Lhuillier, P. Guyot-Sionnest, *IEEE J. Select. Topics Quantum Electron.* **2017**, *23*, 1.
[54] E. Lhuillier, S. Keuleyan, H. Liu, P. Guyot-Sionnest, *Chem. Mater.* **2013**, *25*, 1272.
[55] S. Zhang, Y. Hu, Q. Hao, *Coatings* **2020**, *10*, 760.
[56] E. Lhuillier, S. Keuleyan, P. Guyot-Sionnest, *Nanotechnology* **2012**, *23*, 175705.
[57] M. P. Hendricks, M. P. Campos, G. T. Cleveland, I. Jen-La Plante, J. S. Owen, *Science* **2015**, *348*, 1226.
[58] M. P. Campos, M. P. Hendricks, A. N. Beecher, W. Walravens, R. A. Swain, G. T. Cleveland, Z. Hens, M. Y. Sfeir, J. S. Owen, *J. Am. Chem. Soc.* **2017**, *139*, 2296.
[59] G. Shen, M. Chen, P. Guyot-Sionnest, *J. Phys. Chem. Lett.* **2017**, *8*, 2224.
[60] https://sites.dartmouth.edu/toxmetal/about-us/a-tribute-to-karen-wetterhahn/ visited on 07/12/2024.
[61] N. Goubet, M. Thomas, C. Gréboval, A. Chu, J. Qu, P. Rastogi, S.-S. Chee, M. Goyal, Y. Zhang, X. Z. Xu, G. Cabailh, S. Ithurria, E. Lhuillier, *J. Phys. Chem. C* **2020**, *124*, 8423.
[62] J. Yang, H. Hu, Y. Lv, M. Yuan, B. Wang, Z. He, S. Chen, Y. Wang, Z. Hu, M. Yu, X. Zhang, J. He, J. Zhang, H. Liu, H.-Y. Hsu, J. Tang, H. Song, X. Lan, *Nano Lett.* **2022**, *22*, 3465.
[63] S.-S. Chee, C. Gréboval, D. V. Magalhaes, J. Ramade, A. Chu, J. Qu, P. Rastogi, A. Khalili, T. H. Dang, C. Dabard, Y. Prado, G. Patriarche, J. Chaste, M. Rosticher, S. Bals, C. Delerue, E. Lhuillier, *Nano Lett.* **2021**, *21*, 4145.
[64] B. Wang, H. Hu, M. Yuan, J. Yang, J. Liu, L. Gao, J. Zhang, J. Tang, X. Lan, *Small Methods* **2024**, 2301557.
[65] L. De Trizio, L. Manna, *Chem. Rev.* **2016**, *116*, 10852.
[66] S. Gupta, S. V. Kershaw, A. L. Rogach, *Adv. Mater.* **2013**, *25*, 6923.
[67] H. Zhang, P. Guyot-Sionnest, *J. Phys. Chem. Lett.* **2020**, *11*, 6860.
[68] H. Yang, Q. Zhang, R. Chang, Z. Wu, H. Shen, *Inorg. Chem.* **2024**, *63*, 6231.
[69] K. Xia, G. T. Fei, S. H. Xu, X. D. Gao, Y. F. Liang, *Inorg. Chem.* **2023**, *62*, 13632.
[70] M. Chen, X. Lan, X. Tang, Y. Wang, M. H. Hudson, D. V. Talapin, P. Guyot-Sionnest, *ACS Photonics* **2019**, *6*, 2358.
[71] Y. Prado, J. Qu, C. Gréboval, C. Dabard, P. Rastogi, A. Chu, A. Khalili, X. Z. Xu, C. Delerue, S. Ithurria, E. Lhuillier, *Chem. Mater.* **2021**, *33*, 2054.
[72] Y. Jun, J. Choi, J. Cheon, *Angew. Chem. Int. Ed.* **2006**, *45*, 3414.
[73] G. A. Drake, L. P. Keating, M. Shim, *Chem. Rev.* **2023**, *123*, 3761.
[74] L. Liu, B. Bai, X. Yang, Z. Du, G. Jia, *Chem. Rev.* **2023**, *123*, 3625.
[75] K. E. Shulenberger, M. R. Jilek, S. J. Sherman, B. T. Hohman, G. Dukovic, *Chem. Rev.* **2023**, *123*, 3852.
[76] A. M. Smith, L. A. Lane, S. Nie, *Nat. Commun.* **2014**, *5*, 4506.

[77] C. Dabard, J. Planelles, H. Po, E. Izquierdo, L. Makke, C. Gréboval, N. Moghaddam, A. Khalili, T. H. Dang, A. Chu, S. Pierini, C. Abadie, M. Cavallo, E. Bossavit, X. Z. Xu, P. Hollander, M. Silly, E. Lhuillier, J. I. Climente, S. Ithurria, *Chem. Mater.* **2021**, *33*, 9252.
[78] I. Rosina, B. Martín-García, D. Spirito, Z. Dang, G. Gariano, S. Marras, M. Prato, R. Krahne, L. De Trizio, L. Manna, *Chem. Mater.* **2020**, *32*, 2978.
[79] A. V. Sokolova, I. D. Skurlov, A. A. Babaev, P. S. Perfenov, M. A. Miropoltsev, D. V. Danilov, M. A. Baranov, I. E. Kolesnikov, A. V. Koroleva, E. V. Zhizhin, A. P. Litvin, A. V. Fedorov, S. A. Cherevkov, *Nanomaterials* **2022**, *12*, 4198.
[80] C. Livache, E. Izquierdo, B. Martinez, M. Dufour, D. Pierucci, S. Keuleyan, H. Cruguel, L. Becerra, J. L. Fave, H. Aubin, A. Ouerghi, E. Lacaze, M. G. Silly, B. Dubertret, S. Ithurria, E. Lhuillier, *Nano Lett.* **2017**, *17*, 4067.
[81] C. Dabard, E. Bossavit, T. H. Dang, N. Ledos, M. Cavallo, A. Khalili, H. Zhang, R. Alchaar, G. Patriarche, A. Vasanelli, B. T. Diroll, A. Degiron, E. Lhuillier, S. Ithurria, *J. Phys. Chem. C* **2023**, *127*, 14847.
[82] M. Chen, H. Lu, N. M. Abdelazim, Y. Zhu, Z. Wang, W. Ren, S. V. Kershaw, A. L. Rogach, N. Zhao, *ACS Nano* **2017**, *11*, 5614.
[83] S. Pierini, C. Abadie, T. H. Dang, A. Khalili, H. Zhang, M. Cavallo, Y. Prado, B. Gallas, S. Ithurria, S. Sauvage, J. F. Dayen, G. Vincent, E. Lhuillier, *Mater* **2023**, *16*, 2335.
[84] C. Gréboval, U. Noumbe, N. Goubet, C. Livache, J. Ramade, J. Qu, A. Chu, B. Martinez, Y. Prado, S. Ithurria, A. Ouerghi, H. Aubin, J.-F. Dayen, E. Lhuillier, *Nano Lett.* **2019**, *19*, 3981.
[85] C. Gréboval, A. Chu, D. V. Magalhaes, J. Ramade, J. Qu, P. Rastogi, A. Khalili, S.-S. Chee, H. Aubin, G. Vincent, S. Bals, C. Delerue, E. Lhuillier, *ACS Photonics* **2021**, *8*, 259.
[86] M. Cavallo, E. Bossavit, S. Matzen, T. Maroutian, R. Alchaar, T. H. Dang, A. Khalili, C. Dabard, H. Zhang, Y. Prado, C. Abadie, J. K. Utterback, J. F. Dayen, M. G. Silly, P. Dudin, J. Avila, E. Lhuillier, D. Pierucci, *Adv. Funct. Mater.* **2023**, *33*, 2300846.
[87] M. Cavallo, R. Alchaar, E. Bossavit, H. Zhang, T. H. Dang, A. Khalili, Y. Prado, M. G. Silly, J. K. Utterback, S. Ithurria, P. Dudin, J. Avila, D. Pierucci, E. Lhuillier, *Nanoscale* **2023**, *15*, 9440.
[88] A. Chu, B. Martinez, S. Ferré, V. Noguier, C. Gréboval, C. Livache, J. Qu, Y. Prado, N. Casaretto, N. Goubet, H. Cruguel, L. Dudy, M. G. Silly, G. Vincent, E. Lhuillier, *ACS Appl. Mater. Interfaces* **2019**, *11*, 33116.
[89] G. Shen, P. Guyot-Sionnest, *J. Phys. Chem. C* **2016**, *120*, 11744.
[90] A. L. Rogach, M. T. Harrison, S. V. Kershaw, A. Kornowski, M. G. Burt, A. Eychmüller, H. Weller, *Phys. Stat. Sol.* **2001**, *224*, 153.
[91] N. Gaponik, D. V. Talapin, A. L. Rogach, A. Eychmüller, H. Weller, *Nano Lett.* **2002**, *2*, 803.
[92] N. M. Abdelazim, Q. Zhu, Y. Xiong, Y. Zhu, M. Chen, N. Zhao, S. V. Kershaw, A. L. Rogach, *Chem. Mater.* **2017**, *29*, 7859.
[93] S. V. Kershaw, W. K. Yiu, A. Sergeev, A. L. Rogach, *Chem. Mater.* **2020**, *32*, 3930.
[94] K. S. Jeong, Z. Deng, S. Keuleyan, H. Liu, P. Guyot-Sionnest, *J. Phys. Chem. Lett.* **2014**, *5*, 1139.
[95] G. Shen, P. Guyot-Sionnest, *Chem. Mater.* **2019**, *31*, 286.
[96] A. Kamath, C. Melnychuk, P. Guyot-Sionnest, *J. Am. Chem. Soc.* **2021**, *143*, 19567.
[97] P. Guyot-Sionnest, M. M. Ackerman, X. Tang, *J. Chem. Phys.* **2019**, *151*, 060901.
[98] Q. Wen, S. V. Kershaw, S. Kalytchuk, O. Zhovtiuk, C. Reckmeier, M. I. Vasilevskiy, A. L. Rogach, *ACS Nano* **2016**, *10*, 4301.
[99] S. Keuleyan, J. Kohler, P. Guyot-Sionnest, *J. Phys. Chem. C* **2014**, *118*, 2749.
[100] H. Liu, P. Guyot-Sionnest, *J. Phys. Chem. C* **2010**, *114*, 14860.
[101] C. Melnychuk, P. Guyot-Sionnest, *Chem. Rev.* **2021**, *121*, 2325.
[102] Y.-S. Park, W. K. Bae, J. M. Pietryga, V. I. Klimov, *ACS Nano* **2014**, *8*, 7288.
[103] M. A. Leontiadou, A. Al-Otaify, S. V. Kershaw, O. Zhovtiuk, S. Kalytchuk, D. Mott, S. Maenosono, A. L. Rogach, D. J. Binks, *Chem. Phys.* **2016**, *469*, 25.
[104] C. Melnychuk, P. Guyot-Sionnest, *J. Phys. Chem. Lett.* **2018**, *9*, 2208.
[105] Z. Deng, P. Guyot-Sionnest, *ACS Nano* **2016**, *10*, 2121.
[106] A. Kamath, R. D. Schaller, P. Guyot-Sionnest, *J. Am. Chem. Soc.* **2023**, *145*, 10809.
[107] B. Martinez, C. Livache, N. Goubet, A. Jagtap, H. Cruguel, A. Ouerghi, E. Lacaze, M. G. Silly, E. Lhuillier, *J. Phys. Chem. C* **2018**, *122*, 859.
[108] K. A. Sergeeva, S. Hu, A. V. Sokolova, A. S. Portniagin, D. Chen, S. V. Kershaw, A. L. Rogach, *Adv. Mater.* **2023**, *36*, 2306518.
[109] E. Bossavit, T. H. Dang, P. He, M. Cavallo, A. Khalili, C. Dabard, H. Zhang, D. Gacemi, M. G. Silly, C. Abadie, B. Gallas, D. Pierucci, Y. Todorov, C. Sirtori, B. T. Diroll, A. Degiron, E. Lhuillier, A. Vasanelli, *Adv. Opt. Mater.* **2023**, *11*, 2300863.
[110] S. Pradhan, F. Di Stasio, Y. Bi, S. Gupta, S. Christodoulou, A. Stavrinadis, G. Konstantatos, *Nat. Nanotechnol.* **2019**, *14*, 72.
[111] C. Livache, N. Goubet, C. Gréboval, B. Martinez, J. Ramade, J. Qu, A. Triboulin, H. Cruguel, B. Baptiste, S. Klotz, G. Fishman, S. Sauvage, F. Capitani, E. Lhuillier, *J. Phys. Chem. C* **2019**, *123*, 13122.
[112] S. Pierini, F. Capitani, M. Scimeca, S. Kozlov, D. Pierucci, R. Alchaar, C. Abadie, A. Khalili, M. Cavallo, T. H. Dang, H. Zhang, E. Bossavit, C. Gréboval, J. Avila, B. Baptiste, S. Klotz, A. Sahu, C. Feuillet-Palma, X. Z. Xu, A. Ouerghi, S. Ithurria, J. K. Utterback, S. Sauvage, E. Lhuillier, *J. Phys. Chem. Lett.* **2022**, *13*, 6919.
[113] N. Moghaddam, C. Gréboval, J. Qu, A. Chu, P. Rastogi, C. Livache, A. Khalili, X. Z. Xu, B. Baptiste, S. Klotz, G. Fishman, F. Capitani, S. Ithurria, S. Sauvage, E. Lhuillier, *J. Phys. Chem. C* **2020**, *124*, 23460.
[114] N. Orlowski, J. Augustin, Z. Gołacki, C. Janowitz, R. Manzke, *Phys. Rev. B* **2000**, *61*, R5058.
[115] S. H. Groves, R. N. Brown, C. R. Pidgeon, *Phys. Rev.* **1967**, *161*, 779.
[116] G. L. Hansen, J. L. Schmit, T. N. Casselman, *J. Appl. Phys.* **1982**, *53*, 7099.
[117] A. Hao, C. Gao, M. Li, C. He, X. Huang, D. Zhang, C. Yu, H. Liu, Y. Ma, Y. Tian, G. Zou, *J. Phys.: Condens. Matter* **2007**, *19*, 425222.
[118] S. Einfeldt, F. Goschenhofer, C. R. Becker, G. Landwehr, *Phys. Rev. B* **1995**, *51*, 4915.
[119] S. L. Lehoczky, J. G. Broerman, D. A. Nelson, C. R. Whitsett, *Phys. Rev. B* **1974**, *9*, 1598.
[120] M. Von Truchseß, A. Pfeuffer-Jeschke, C. R. Becker, G. Landwehr, E. Batke, *Phys. Rev. B* **2000**, *61*, 1666.
[121] K.-U. Gawlik, L. Kipp, M. Skibowski, N. Orłowski, R. Manzke, *Phys. Rev. Lett.* **1997**, *78*, 3165.
[122] R. Zallen, M. Slade, *Solid State Commun.* **1970**, *8*, 1291.
[123] K. Dybko, W. Szuszkiewicz, E. Dynowska, W. Paszkowicz, B. Witkowska, *Phys. B* **1998**, *256*, 629.
[124] G. Allan, C. Delerue, *Phys. Rev. B* **2012**, *86*, 165437.
[125] E. Kalesaki, W. H. Evers, G. Allan, D. Vanmaekelbergh, C. Delerue, *Phys. Rev. B* **2013**, *88*, 115431.
[126] A. Svane, N. E. Christensen, M. Cardona, A. N. Chantis, M. Van Schilfgaarde, T. Kotani, *Phys. Rev. B* **2011**, *84*, 205205.
[127] R. Sakuma, C. Friedrich, T. Miyake, S. Blügel, F. Aryasetiawan, *Phys. Rev. B* **2011**, *84*, 085144.
[128] J. P. Laurenti, J. Camassel, A. Bouhemadou, B. Toulouse, R. Legros, A. Lusson, *J. Appl. Phys.* **1990**, *67*, 6454.
[129] V. Latussek, C. R. Becker, G. Landwehr, R. Bini, L. Ulivi, *Phys. Rev. B* **2005**, *71*, 125305.
[130] N. G. Wright, M. I. McMahon, R. J. Nelmes, A. San-Miguel, *Phys. Rev. B* **1993**, *48*, 13111.
[131] P. Man, D. S. Pan, *Phys. Rev. B* **1991**, *44*, 8745.
[132] J. W. Nicklas, J. W. Wilkins, *Phys. Rev. B* **2011**, *84*, 121308.

[133] Y. Guldner, C. Rigaux, M. Grynberg, A. Mycielski, *Phys. Rev. B* **1973**, *8*, 3875.
[134] Y. Guldner, C. Rigaux, A. Mycielski, Y. Couder, *Phys. Status Solidi B* **1977**, *81*, 615.
[135] X. C. Zhang, A. Pfeuffer-Jeschke, K. Ortner, V. Hock, H. Buhmann, C. R. Becker, G. Landwehr, *Phys. Rev. B* **2001**, *63*, 245305.
[136] D. J. Chadi, J. P. Walter, M. L. Cohen, Y. Petroff, M. Balkanski, *Phys. Rev. B* **1972**, *5*, 3058.
[137] S. Meçabih, N. Amrane, B. Belgoumène, H. Aourag, *Phys. A* **2000**, *276*, 495.
[138] J.-W. Luo, A. Zunger, *Phys. Rev. Lett.* **2010**, *105*, 176805.
[139] M. Penna, A. Marnetto, F. Bertazzi, E. Bellotti, M. Goano, *J. Electron. Mater.* **2009**, *38*, 1717.
[140] J. N. Schulman, Y.-C. Chang, *Phys. Rev. B* **1986**, *33*, 2594.
[141] C. J. Delerue, M. Lannoo, *Nanostructures: theory and modeling*, Springer, New York, **2004**.
[142] W. D. Lawson, S. Nielsen, E. H. Putley, A. S. Young, *J. Phys. Chem. Solids* **1959**, *9*, 325.
[143] J. Camassel, J. P. Laurenti, A. Bouhemadou, R. Legros, A. Lusson, B. Toulouse, *Phys. Rev. B* **1988**, *38*, 3948.
[144] X.-L. Qi, S.-C. Zhang, *Rev. Mod. Phys.* **2011**, *83*, 1057.
[145] B. A. Bernevig, T. L. Hughes, S.-C. Zhang, *Science* **2006**, *314*, 1757.
[146] F. Kirtschig, J. Van Den Brink, C. Ortix, *Phys. Rev. B* **2016**, *94*, 235437.
[147] C. Brüne, C. X. Liu, E. G. Novik, E. M. Hankiewicz, H. Buhmann, Y. L. Chen, X. L. Qi, Z. X. Shen, S. C. Zhang, L. W. Molenkamp, *Phys. Rev. Lett.* **2011**, *106*, 126803.
[148] A. Rogalski, *Opto-Electron. Rev.* **2012**, *20*, 279.
[149] K. Chang, W.-K. Lou, *Phys. Rev. Lett.* **2011**, *106*, 206802.
[150] X. W. Zhang, J. B. Xia, *J. Phys. D: Appl. Phys.* **2006**, *39*, 1815.
[151] B. Puzantian, Y. Saleem, M. Korkusinski, P. Hawrylak, *Nanomaterials* **2022**, *12*, 4283.
[152] J. Li, D. Zhang, J.-J. Zhu, *Phys. E* **2017**, *93*, 58.
[153] M. H. Hudson, M. Chen, V. Kamysbayev, E. M. Janke, X. Lan, G. Allan, C. Delerue, B. Lee, P. Guyot-Sionnest, D. V. Talapin, *ACS Nano* **2018**, *12*, 9397.
[154] N. Malkova, G. W. Bryant, *Phys. Rev. B* **2010**, *82*, 155314.
[155] W. Beugeling, E. Kalesaki, C. Delerue, Y.-M. Niquet, D. Vanmaekelbergh, C. M. Smith, *Nat. Commun.* **2015**, *6*, 6316.
[156] A. Tadjine, Y.-M. Niquet, C. Delerue, *Phys. Rev. B* **2017**, *95*, 235437.
[157] V. Rinnerbauer, K. Hingerl, M. Kovalenko, W. Heiss, *Appl. Phys. Lett.* **2006**, *89*, 193114.
[158] P. Geiregat, A. J. Houtepen, L. K. Sagar, I. Infante, F. Zapata, V. Grigel, G. Allan, C. Delerue, D. Van Thourhout, Z. Hens, *Nat. Mater.* **2018**, *17*, 35.
[159] A. Al-Otaify, S. V. Kershaw, S. Gupta, A. L. Rogach, G. Allan, C. Delerue, D. J. Binks, *Phys. Chem. Chem. Phys.* **2013**, *15*, 16864.
[160] P. Rastogi, E. Izquierdo, C. Gréboval, M. Cavallo, A. Chu, T. H. Dang, A. Khalili, C. Abadie, R. Alchaar, S. Pierini, H. Cruguel, N. Witkowski, J. K. Utterback, T. Brule, X. Z. Xu, P. Hollander, A. Ouerghi, B. Gallas, M. G. Silly, E. Lhuillier, *J. Phys. Chem. C* **2022**, *126*, 13720.
[161] J. Yang, Y. Lv, Z. He, B. Wang, S. Chen, F. Xiao, H. Hu, M. Yu, H. Liu, X. Lan, H.-Y. Hsu, H. Song, J. Tang, *ACS Photonics* **2023**, *10*, 2226.
[162] X. Tang, M. M. Ackerman, M. Chen, P. Guyot-Sionnest, *Nat. Photonics* **2019**, *13*, 277.
[163] A. Chu, C. Gréboval, Y. Prado, H. Majjad, C. Delerue, J.-F. Dayen, G. Vincent, E. Lhuillier, *Nat. Commun* **2021**, *12*, 1.
[164] A. Chu, C. Gréboval, N. Goubet, B. Martinez, C. Livache, J. Qu, P. Rastogi, F. A. Bresciani, Y. Prado, S. Suffit, S. Ithurria, G. Vincent, E. Lhuillier, *ACS Photonics* **2019**, *6*, 2553.
[165] M. Chen, L. Lu, H. Yu, C. Li, N. Zhao, *Adv. Sci.* **2021**, *8*, 2101560.
[166] N. Yan, Y. Qiu, X. He, X. Tang, Q. Hao, M. Chen, *Mater* **2023**, *16*, 3216.
[167] C. Wang, J. Roither, R. Kirschschlager, M. V. Kovalenko, M. Brehm, T. Fromherz, Q. Kan, P. Tan, J. Liu, H. Chen, W. Heiss, *Appl. Phys. Lett.* **2009**, *95*, 053107.
[168] J. Roither, M. V. Kovalenko, S. Pichler, T. Schwarzl, W. Heiss, *Appl. Phys. Lett.* **2005**, *86*, 241104.
[169] X. Tang, M. M. Ackerman, G. Shen, P. Guyot-Sionnest, *Small* **2019**, *15*, 1804920.
[170] Y. Yifat, M. Ackerman, P. Guyot-Sionnest, *Appl. Phys. Lett.* **2017**, *110*, 041106.
[171] Y. Qiu, N. Yan, H. Yao, M. Chen, *Infrared Phys. Technol.* **2023**, *135*, 104980.
[172] T. H. Dang, C. Abadie, A. Khalili, C. Gréboval, H. Zhang, Y. Prado, X. Z. Xu, D. Gacemi, A. Descamps-Mandine, S. Ithurria, Y. Todorov, C. Sirtori, A. Vasanelli, E. Lhuillier, *Adv. Opt. Mater.* **2022**, *10*, 2200297.
[173] X. Tang, M. M. Ackerman, P. Guyot-Sionnest, *Laser Photonics Rev.* **2019**, *13*, 1900165.
[174] T. H. Dang, A. Vasanelli, Y. Todorov, C. Sirtori, Y. Prado, A. Chu, C. Gréboval, A. Khalili, H. Cruguel, C. Delerue, G. Vincent, E. Lhuillier, *Nano Lett.* **2021**, *21*, 6671.
[175] A. Chu, C. Gréboval, N. Goubet, B. Martinez, C. Livache, J. Qu, P. Rastogi, F. A. Bresciani, Y. Prado, S. Suffit, S. Ithurria, G. Vincent, E. Lhuillier, *ACS Photonics* **2019**, *6*, 2553.
[176] A. Khalili, M. Weis, S. G. Mizrahi, A. Chu, T. H. Dang, C. Abadie, C. Gréboval, C. Dabard, Y. Prado, X. Z. Xu, E. Péronne, C. Livache, S. Ithurria, G. Patriarche, J. Ramade, G. Vincent, D. Boschetto, E. Lhuillier, *ACS Photonics* **2022**, *9*, 985.
[177] P. Rastogi, A. Chu, T. H. Dang, Y. Prado, C. Gréboval, J. Qu, C. Dabard, A. Khalili, E. Dandeu, B. Fix, X. Z. Xu, S. Ithurria, G. Vincent, B. Gallas, E. Lhuillier, *Adv. Opt. Mater.* **2021**, *9*, 2002066.
[178] T. H. Dang, C. Abadie, A. Chu, M. Cavallo, A. Khalili, C. Dabard, E. Bossavit, H. Zhang, Y. Prado, D. Pierucci, J. K. Utterback, Y. Todorov, C. Sirtori, J. Jaeck, G. Vincent, A. Vasanelli, B. Fix, E. Lhuillier, *ACS Photonics* **2023**, *10*, 1601.
[179] Y. Ning, S. Zhang, Y. Hu, Q. Hao, X. Tang, *Coatings* **2020**, *10*, 1218.
[180] B. Zhu, M. Chen, Q. Zhu, G. Zhou, N. M. Abdelazim, W. Zhou, S. V. Kershaw, A. L. Rogach, N. Zhao, H. K. Tsang, *Adv. Mater. Technol.* **2019**, *4*, 1900354.
[181] C. Abadie, L. Paggi, A. Fabas, A. Khalili, T. H. Dang, C. Dabard, M. Cavallo, R. Alchaar, H. Zhang, Y. Prado, N. Bardou, C. Dupuis, X. Z. Xu, S. Ithurria, D. Pierucci, J. K. Utterback, B. Fix, G. Vincent, P. Bouchon, E. Lhuillier, *Nano Lett.* **2022**, *22*, 8779.
[182] C. Abadie, L. Paggi, A. Fabas, A. Khalili, T. H. Dang, C. Dabard, M. Cavallo, R. Alchaar, H. Zhang, Y. Prado, N. Bardou, C. Dupuis, X. Z. Xu, S. Ithurria, D. Pierucci, J. K. Utterback, B. Fix, G. Vincent, P. Bouchon, E. Lhuillier, *Nano Lett.* **2022**, *22*, 8779.
[183] J. C. Peterson, P. Guyot-Sionnest, *ACS Appl. Mater. Interfaces* **2023**, *15*, 19163.
[184] P. Zhao, G. Mu, M. Chen, X. Tang, *Coatings* **2022**, *12*, 499.
[185] H.-L. Chen, A. Cattoni, R. De Lépinau, A. W. Walker, O. Höhn, D. Lackner, G. Siefer, M. Faustini, N. Vandamme, J. Goffard, B. Behaghel, C. Dupuis, N. Bardou, F. Dimroth, S. Collin, *Nat. Energy* **2019**, *4*, 761.
[186] T. H. Dang, A. Khalili, C. Abadie, C. Gréboval, M. Cavallo, H. Zhang, E. Bossavit, J. K. Utterback, E. Dandeu, Y. Prado, G. Vincent, S. Ithurria, Y. Todorov, C. Sirtori, A. Vasanelli, E. Lhuillier, *ACS Photonics* **2022**, *9*, 2528.
[187] N. Ledos, T. H. Dang, M. Cavallo, H. Zhang, E. Bossavit, A. Khalili, L. N. Do, C. Gréboval, S. Ithurria, J. K. Utterback, D. Pierucci, G. Vincent, A. Vasanelli, E. Lhuillier, *Adv. Mater. Technol.* **2024**, 2301463.
[188] S. B. Hafiz, M. Scimeca, A. Sahu, D.-K. Ko, *Nano Convergence* **2019**, *6*, 7.
[189] T. Nakotte, S. G. Munyan, J. W. Murphy, S. A. Hawks, S. Kang, J. Han, A. M. Hiszpanski, *J. Mater. Chem. C* **2022**, *10*, 790.
[190] N. Huo, S. Gupta, G. Konstantatos, *Adv. Mater.* **2017**, *29*, 1606576.
[191] A. Rogalski, *J. Alloys Compd.* **2004**, *371*, 53.
[192] C. Cervera, N. Baier, O. Gravrand, L. Mollard, C. Lobre, G. Destefanis, J. P. Zanatta, O. Boulade, V. Moreau, (Eds.: B. F. Andresen, G. F. Fulop, C. M. Hanson), Norton, P. R **2015**, 945129.

[193] J. Kaniewski, J. Piotrowski, *Opto-Electron. Rev.* **2004**, *12*, 139.
[194] H. Xia, T.-X. Li, H.-J. Tang, L. Zhu, X. Li, H.-M. Gong, W. Lu, *Sci. Rep.* **2016**, *6*, 21544.
[195] I. Kanno, S. Hishiki, O. Sugiura, R. Xiang, T. Nakamura, M. Katagiri, *Nuc. Instrum. Methods in Phys. Research* **2006**, *568*, 416.
[196] Q. Meng, X. Zhang, Y. Lü, J. Si, *Opt. Quantum Electron.* **2017**, *49*, 402.
[197] H. C. Liu, A. G. Steele, M. Buchanan, Z. R. Wasilewski, *J. Appl. Phys.* **1993**, *73*, 2029.
[198] H. Schneider, H. C. Liu, *Quantum Well Infrared Photodetectors* **2007**.
[199] V. Gueriaux, N. B. de l'Isle, A. Berurier, O. Huet, A. Manissadjian, H. Facoetti, X. Marcadet, M. Carras, V. Trinité, A. Nedelcu, *Opt. Eng* **2011**, *50*, 061013.
[200] A. Haddadi, A. Dehzangi, R. Chevallier, S. Adhikary, M. Razeghi, *Sci. Rep.* **2017**, *7*, 3379.
[201] A. Haddadi, R. Chevallier, G. Chen, A. M. Hoang, M. Razeghi, *Appl. Phys. Lett.* **2015**, *106*, 011104.
[202] P. Guyot-Sionnest, J. A. Roberts, *Appl. Phys. Lett.* **2015**, *107*, 253104.
[203] R. Alchaar, C. Dabard, D. Mastrippolito, E. Bossavit, T. H. Dang, M. Cavallo, A. Khalili, H. Zhang, L. Domenach, N. Ledos, Y. Prado, D. Troadec, J. Dai, M. Tallarida, F. Bisti, F. Cadiz, G. Patriarche, J. Avila, E. Lhuillier, D. Pierucci, *J. Phys. Chem. C* **2023**, *127*, 12218.
[204] M. M. Ackerman, X. Tang, P. Guyot-Sionnest, *ACS Nano* **2018**, *12*, 7264.
[205] M. M. Ackerman, M. Chen, P. Guyot-Sionnest, *Appl. Phys. Lett.* **2020**, *116*, 083502.
[206] C. Gréboval, E. Izquierdo, C. Abadie, A. Khalili, M. Cavallo, A. Chu, T. H. Dang, H. Zhang, X. Lafosse, M. Rosticher, X. Z. Xu, A. Descamps-Mandine, A. Ouerghi, M. G. Silly, S. Ithurria, E. Lhuillier, *ACS Appl. Nano Mater* **2022**, *5*, 8602.
[207] A. J. Ciani, R. E. Pimpinella, C. H. Grein, P. Guyot-Sionnest, in *ITechnology and AXLII*, (Eds.: B. F. Andresen; G. F. Fulop, C. M. Hanson, J. L. Miller), Norton, P. R **2016**, 981919.
[208] T. Yimei, Z. Shuo, L. Yuning, H. Qun, C. Menglu, L. Yanfei, T. Xin, *Infrar. Laser Engineer.* **2023**, *52*, 20230377.
[209] T. Yimei, X. Yingying, Z. Shuo, L. Yanfei, H. Qun, T. Xin, *Laser Optoelectron. Prog.* **2023**, *61*, 0211006.
[210] U. N. Noumbé, C. Gréboval, C. Livache, A. Chu, H. Majjad, L. E. Parra López, L. D. N. Mouafo, B. Doudin, S. Berciaud, J. Chaste, A. Ouerghi, E. Lhuillier, J.-F. Dayen, *ACS Nano* **2020**, *14*, 4567.
[211] C. Gréboval, C. Dabard, N. Konstantinov, M. Cavallo, S.-S. Chee, A. Chu, T. H. Dang, A. Khalili, E. Izquierdo, Y. Prado, H. Majjad, X. Z. Xu, J.-F. Dayen, E. Lhuillier, *ACS Appl. Electron. Mater.* **2021**, *3*, 4681.
[212] Y. Luo, Y. Tan, C. Bi, S. Zhang, X. Xue, M. Chen, Q. Hao, Y. Liu, X. Tang, *APL Photonics* **2023**, *8*, 056109.
[213] S. Zhang, C. Bi, Y. Tan, Y. Luo, Y. Liu, J. Cao, M. Chen, Q. Hao, X. Tang, *ACS Nano* **2022**, *16*, 18822.
[214] Y. Luo, S. Zhang, X. Tang, M. Chen, *J. Mater. Chem. C* **2022**, *10*, 8218.
[215] S. Zhang, G. Mu, J. Cao, Y. Luo, Q. Hao, M. Chen, Y. Tan, P. Zhao, X. Tang, *Photon. Res.* **2022**, *10*, 1987.
[216] X. Tang, M. Chen, A. Kamath, M. M. Ackerman, P. Guyot-Sionnest, *ACS Photonics* **2020**, *7*, 1117.
[217] P. Zhao, T. Qin, G. Mu, S. Zhang, Y. Luo, M. Chen, X. Tang, *J. Mater. Chem. C* **2023**, *11*, 2842.
[218] E. Lhuillier, A. Robin, S. Ithurria, H. Aubin, B. Dubertret, *Nano Lett.* **2014**, *14*, 2715.
[219] P. Zhao, G. Mu, C. Wen, Y. Qi, H. Lv, X. Tang, *Physica Rapid Research Ltrs* **2023**, 2300121.
[220] G. Mu, T. Rao, S. Zhang, C. Wen, M. Chen, Q. Hao, X. Tang, *ACS Appl. Mater. Interfaces* **2022**, *14*, 45553.
[221] T. J. Sanders, G. T. Hess, (Eds: B. F. Andresen, G. F. Fulop), Orlando, FL, **2003**, 138.
[222] E. Georgitzikis, P. E. Malinowski, Y. Li, J. Maes, L. M. Hagelsieb, S. Guerrieri, Z. Hens, P. Heremans, D. Cheyns, *IEEE Sensors J.* **2020**, *20*, 6841.
[223] J. S. Steckel, E. Josse, A. G. Pattantyus-Abraham, M. Bidaud, B. Mortini, H. Bilgen, O. Arnaud, S. Allegret-Maret, F. Saguin, L. Mazet, S. Lhostis, T. Berger, K. Haxaire, L. L. Chapelon, L. Parmigiani, P. Gouraud, M. Brihoum, P. Bar, M. Guillermet, S. Favreau, R. Duru, J. Fantuz, S. Ricq, D. Ney, I. Hammad, D. Roy, A. Arnaud, B. Vianne, G. Nayak, N. Virollet, et al., In *2021 IEEE International Electron Devices Meeting (IEDM)*, IEEE, San Francisco, CA, USA, **2021**.
[224] A. Gupta, J. C. Ondry, M. Chen, M. H. Hudson, I. Coropceanu, N. A. Sarma, D. V. Talapin, *Nano Lett.* **2022**, *22*, 6545.
[225] L. Asor, J. Liu, Y. Ossia, D. C. Tripathi, N. Tessler, A. I. Frenkel, U. Banin, *Adv. Funct. Materials* **2021**, *31*, 2007456.
[226] L. Asor, J. Liu, S. Xiang, N. Tessler, A. I. Frenkel, U. Banin, *Adv. Mater.* **2023**, *35*, 2208332.
[227] D. Mocatta, G. Cohen, J. Schattner, O. Millo, E. Rabani, U. Banin, *Science* **2011**, *332*, 77.
[228] A. Gupta, J. C. Ondry, K. Lin, Y. Chen, M. H. Hudson, M. Chen, R. D. Schaller, A. J. Rossini, E. Rabani, D. V. Talapin, *J. Am. Chem. Soc.* **2023**, *145*, 16429.
[229] A. Saha, R. Yadav, D. Aldakov, P. Reiss, *Angew. Chem. Int. Ed.* **2023**, *62*, 202311317.
[230] L. Peng, Y. Wang, Y. Ren, Z. Wang, P. Cao, G. Konstantatos, *ACS Nano* **2024**, *18*, 5113.
[231] W. J. Mir, T. Sheikh, S. Nematulloev, P. Maity, K. E. Yorov, A. Emwas, M. N. Hedhili, M. S. Khan, M. Abulikemu, O. F. Mohammed, O. M. Bakr, *Small* **2024**, *20*, 2306535.
[232] Z. Deng, K. S. Jeong, P. Guyot-Sionnest, *ACS Nano* **2014**, *8*, 11707.
[233] A. Sahu, A. Khare, D. D. Deng, D. J. Norris, *Chem. Commun.* **2012**, *48*, 5458.
[234] J. Qu, N. Goubet, C. Livache, B. Martinez, D. Amelot, C. Gréboval, A. Chu, J. Ramade, H. Cruguel, S. Ithurria, M. G. Silly, E. Lhuillier, *J. Phys. Chem. C* **2018**, *122*, 18161.
[235] M. R. Scimeca, N. Mattu, I. J. Paredes, M. N. Tran, S. J. Paul, E. S. Aydil, A. Sahu, *J. Phys. Chem. C* **2021**, *125*, 17556.
[236] M. Park, D. Choi, Y. Choi, H. Shin, K. S. Jeong, *ACS Photonics* **2018**, *5*, 1907.

Kseniia A. Sergeeva is a third-year Ph.D. student under the supervision of Andrey Rogach at the City University of Hong Kong. She obtained an Engineer degree in Optics, followed by a Ph.D. in Condensed Matter Physics and Solid-State Chemistry of transition metal doped silicate luminophores from Ural Federal University in Ekaterinburg, Russia. Her current research interests are dedicated to optical spectroscopy of IR-emitting colloidal nanocrystals, and material and device engineering of HgTe-based photodetectors.

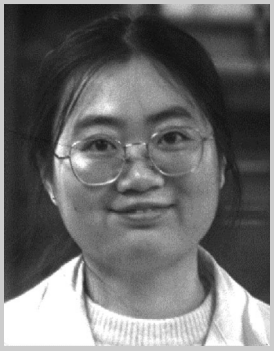

Huichen Zhang is a Ph.D. student at Sorbonne University under the supervision of Emmanuel Lhuillier. She received a bachelor's degree from Nanjing University of Science and Technology and a master's from Nanjing University in China. She is interested in nanocrystal synthesis for infrared optoelectronic devices. Her image is acquired with a HgTe CQDs based camera.

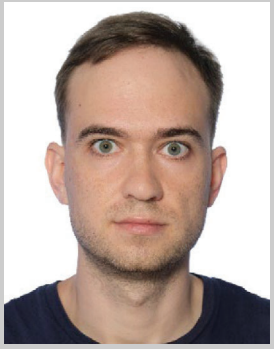

Arsenii S. Portniagin is a post doctoral fellow at City University of Hong Kong. He received his B.Sc. and M.Sc. in Chemistry from Far Eastern Federal University in Vladivostok (Russia), Ph.D. in Physical Chemistry from the Institute of Chemistry FEB RAS in Vladivostok, and Ph.D. in Materials Science in City University of Hong Kong. His current research interests embrace the development of cation-exchange approaches to the synthesis of 1D anisotropic metal chalcogenides, their optical spectroscopy and use for light detection and catalysis.

Erwan Bossavit is a Ph.D. student in a joint project between the INSP laboratory of Sorbonne Université and the SOLEIL synchrotron, supervised by Emmanuel Lhuillier and Mathieu G. Silly. His research interests revolve around the design and implementation of novel infrared-emitting LEDs based on nanocrystals.

Ge Mu is an assistant professor at the Beijing Institute of Technology in the Laboratory of Broadband and Multi-dimensional Optoelectronic Devices. She obtained Ph.D. degree from Beijing Institute of Technology and conducted postdoctoral research supervised by Professor Xin Tang. She is dedicated to the design and application of infrared-to-visible upconversion devices.

Stephen V. Kershaw After his early postdoc. work on liquid crystals in the 1980′s, Steve moved into optoelectronic materials and devices research at British Telecom's Research Laboratories, UK. Initially this work focused on optically nonlinear organic polymers and organo-metallic compounds, but by the late 1990′s infrared CQDs were also included. In 2000, along with former colleagues from BT Labs, Steve founded and managed a small QD company with the aim of commercializing the technology. In 2010, he moved to City University of Hong Kong where he continues to develop IR QD materials and devices.

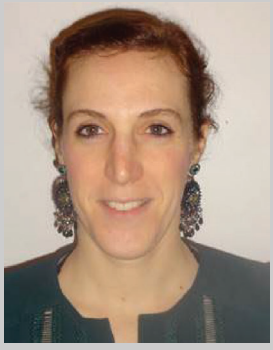

Sandrine Ithurria is an associate professor at the Ecole Supérieure de Physiques et de Chimie Industrielles Paris PSL, in the laboratory of Physics and Materials Studies. She obtained this position in 2012 after a postdoc. at the University of Chicago in the D. Talapin's group. Her research is dedicated to the synthesis and applications of 2D semiconductor nanoparticles from the visible to the infrared range

Philippe Guyot-Sionnest did his Ph.D. on surface non-linear optics with Prof. Yuen Ron Shen at UC Berkeley. Since 1991, he is a professor of physics and chemistry at the University of Chicago. Exploring colloidal nanoparticles, his group introduced bright core/shells, mid-infrared intraband transitions, charge transfer doping, ligand exchange, and recently cascade emission.

Sean Keuleyan earned a bachelor's degree in chemistry at Temple University working with Prof. Eric Borguet. He went on to do a Ph.D. at the University of Chicago, working with Prof. Philippe P. Guyot-Sionnest and Emmanuel Lhuillier on HgTe CQDs for MWIR. After a post-doctoral position at Brown University investigating 2D silicon telluride, he joined Voxtel, Inc. in 2014 and worked on 2D arrays of CQD-based sensors for SWIR and MWIR imaging. In 2020, Voxtel was acquired by Allegro Microsystems, where his work focused on SWIR time of flight LIDAR. In 2023, he joined the Material Solutions division at Entegris Inc.

Christophe Delerue is Director of Research at the CNRS. He is currently a Scientific Director of the Institut d'Electronique, de Microélectronique et de Nanotechnologie (IEMN), which is part of the Université de Lille, CNRS, Université Polytechnique Hauts-de-France, Junia ISEN and Centrale Lille. Author of over 200 articles in international peer-reviewed journals, he is a condensed matter theorist, specializing in numerical modelling, in particular of the electronic properties of semiconductor nanostructures.

Xin Tang obtained his Ph.D. degree from City University of Hong Kong in 2017. He then joined the Guyot-Sionnest group as a post-doctoral scholar at the University of Chicago, where he focused on the study of HgTe CQD infrared detectors. Since 2020, he has been the director of the Laboratory of Broadband and Multi-dimensional Optoelectronic Devices, and a professor at the School of Optics and Photonics of Beijing Institute of Technology, with a research focus on single-band, dual-band, and multispectral CQD focal plane array imagers.

Andrey L. Rogach received his Ph.D. in Chemistry in 1995 from the Belarusian State University in Minsk, and completed his Habilitation in Experimental Physics at the University of Munich, Germany in 2009, moving to Hong Kong in the same year. He is currently Yeung Kin Man Chair Professor in Photonics Materials and Founding Director of the Centre for Functional Photonics at City University of Hong Kong. His research focuses on the synthesis, assembly and optical spectroscopy of semiconductor nanocrystals, and their use for optoelectronic and energy-related applications.

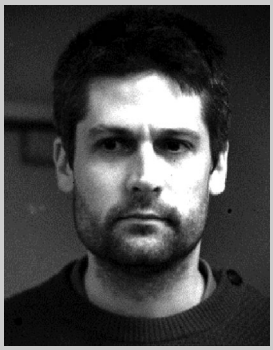

Emmanuel Lhuillier obtained an engineering degree from ESPCI and a master's degree in condensed matter from the Université Pierre and Marie Curie. He did his Ph.D. at Onera (French aerospace lab) under the supervision of Emmanuel Rosencher working on transport properties of quantum wells. He then joined the P. Guyot-Sionnest group as a post-doctoral scholar at the University of Chicago, where he got sensitized to HgTe CQDs. He then conducted a second post-doc at ESPCI in B. Dubertret's group working on optoelectronic properties of colloidal quantum wells. Since 2015, he is a CNRS researcher on optoelectronic of confined nanomaterials in the Institut des NanoSciences de Paris from Sorbonne Université. His image is acquired with a HgTe CQD based camera.